Oceanographic variability in Cumberland Bay, South Georgia, and its implications for glacier retreat

Joanna C Zanker[1], Emma F. Young[1], Paul Richard Holland[1], Ivan D Haigh[2], and Paul Brickle[3]

[1]British Antarctic Survey
[2]University of Southampton
[3]South Atlantic Environmental Research Insitute

March 6, 2023

Abstract

South Georgia is a heavily glaciated sub-Antarctic island in the Southern Ocean. Cumberland Bay is the largest fjord on the island, split into two arms, each with a large marine-terminating glacier at the head. Although these glaciers have shown markedly different retreat rates over the past century, the underlying drivers of such differential retreat are not yet understood. This study uses observations and a new high-resolution oceanographic model to characterize oceanographic variability in Cumberland Bay and to explore its influence on glacier retreat. While observations indicate a strong seasonal cycle in temperature and salinity, they reveal no clear hydrographic differences that could explain the differential glacier retreat. Model simulations suggest the subglacial outflow plume dynamics and fjord circulation are sensitive to the bathymetry adjacent to the glacier. The addition of a postulated shallow inner sill in one fjord arm significantly changes the water properties in the resultant inner basin by blocking the intrusion of colder, higher salinity waters at depth. This increase in temperature could accelerate both the subglacial plume-driven melt, and the melting of the wider submarine ice face, which is proposed as a possible explanation for the different rates of glacier retreat observed in the two fjord arms. This study represents the first detailed description of the oceanographic variability of a sub-Antarctic island fjord, highlighting the sensitivity of plume dynamics to bathymetry. Notably, in fjords systems where temperature decreases with depth, the presence of a shallow sill has the potential to accelerate glacier retreat.

Oceanographic variability in Cumberland Bay, South Georgia, and its implications for glacier retreat

Joanna C. Zanker[1], Emma. Young[1], Paul. R. Holland[1], Ivan D. Haigh[2], Paul Brickle[3]

[1]British Antarctic Survey, Cambridge, UK. [2]Ocean and Earth Science, National Oceanography Centre, University of Southampton, Southampton, UK. [3]South Atlantic Environmental Research Institute, Stanley, FI.

Corresponding author: Joanna C. Zanker (joazan@bas.ac.uk)

Key Points:

- Observational data and a new high-resolution model are combined to describe oceanographic variability in Cumberland Bay, South Georgia.
- We show that buoyancy-driven subglacial outflow plumes are a key driver of seasonal variability and spatial differences between fjord arms.
- We highlight that the presence of a postulated inner sill may be a key factor in the observed rapid glacier retreat.

Abstract

South Georgia is a heavily glaciated sub-Antarctic island in the Southern Ocean. Cumberland Bay is the largest fjord on the island, split into two arms, each with a large marine-terminating glacier at the head. Although these glaciers have shown markedly different retreat rates over the past century, the underlying drivers of such differential retreat are not yet understood. This study uses observations and a new high-resolution oceanographic model to characterize oceanographic variability in Cumberland Bay and to explore its influence on glacier retreat. While observations indicate a strong seasonal cycle in temperature and salinity, they reveal no clear hydrographic differences that could explain the differential glacier retreat. Model simulations suggest the subglacial outflow plume dynamics and fjord circulation are sensitive to the bathymetry adjacent to the glacier. The addition of a postulated shallow inner sill in one fjord arm significantly changes the water properties in the resultant inner basin by blocking the intrusion of colder, higher salinity waters at depth. This increase in temperature could accelerate both the subglacial plume-driven melt, and the melting of the wider submarine ice face, which is proposed as a possible explanation for the different rates of glacier retreat observed in the two fjord arms. This study represents the first detailed description of the oceanographic variability of a sub-Antarctic island fjord, highlighting the sensitivity of plume dynamics to bathymetry. Notably, in fjords systems where temperature decreases with depth, the presence of a shallow sill has the potential to accelerate glacier retreat.

Plain Language Summary

Cumberland Bay, a fjord on the sub-Antarctic island of South Georgia, is split into two arms, each with a large marine-terminating glacier. One of these glaciers is retreating much faster than the other, possibly due to differences in oceanography between the arms. Here, we investigate how the oceanography in Cumberland Bay varies seasonally and with the seabed depth by using oceanographic data and numerical ocean simulations. We find that the properties of buoyant plumes, which arise from meltwater entering the ocean from beneath the glacier, are sensitive to the seabed depth near the glaciers, resulting in strong differences in ocean flow between the fjord arms. Assuming higher ocean temperatures increase glacier melting, we find that the presence of a near-glacier shallow sill likely increases melting by blocking deeper, colder waters and trapping warmer surface waters close to the glacier. As a shallow sill is likely to be present near

the rapidly retreating glacier only, this result offers a persuasive explanation for the observed glacier retreat. Understanding the variability in oceanography and glacier retreat is important as they directly impact the marine ecosystem at South Georgia by influencing the availability of nutrients for primary production and food availability for higher predators.

1 Introduction

Fjords are a common feature of high-latitude coastlines and have high biological productivity. In the Arctic, fjords are found in Alaska, Svalbard, and Greenland, for example. In the Southern Hemisphere, fjords are found in Patagonia, New Zealand, Antarctica, and on sub-Antarctic islands. High-latitude fjords are usually associated with seasonal sea ice and, in most cases, have a glacier terminating at the fjord head (Cottier et al., 2010). Fjord circulation directly governs the stability of tidewater (grounded) glaciers (Cottier et al., 2010), frontal ablation of which directly contributes to sea-level rise (Benn et al., 2017).

Marine ecosystems in fjords support large colonies of higher predators such as sea birds and marine mammals (Ward, 1989; Węsławski et al., 2000), while open ocean and on-shelf phytoplankton blooms may also rely on the transport of nutrients circulated by nearby fjords from upwelling and terrestrial sources via glacial runoff (Holmes et al., 2019; Węsławski et al., 2000). Fjords are also important spawning grounds for fish (Everson et al., 2001). Recruitment and retention of fish larvae are controlled by fjord circulation and shelf exchange, an understanding of which is vital for the management of local fisheries (Everson, 1992). In our changing climate, frontal ablation of tidewater glaciers is expected to increase (Christoffersen et al., 2011; Mortensen et al., 2011; Straneo et al., 2010), the composition and extent of phytoplankton blooms are expected to change substantially (Sommer & Lengfellner, 2008; Winder & Sommer, 2012) and the changes in fjord circulation are likely to impact a diversity of ecosystem responses, such as fish larvae retention (Wesławski et al., 2011). Therefore, understanding fjord systems is crucial.

In this paper, we focus on South Georgia, a sub-Antarctic island in the Southern Ocean which is heavily glaciated and indented with fjords. The island lies in the path of the Antarctic Circumpolar Current (ACC), which flows unimpeded around the Southern Ocean, driven by strong westerly winds (Orsi et al., 1995). The Polar Front lies to the north of the island and the

Southern Antarctic Circumpolar Current Front (SACCF) loops anticyclonically around the island from the south before retroflecting to the east (Fig. 1a) (Meredith et al., 2005). While the island lies beyond the winter sea-ice limit, it does see the formation of intermittent seasonal pancake ice. Cumberland Bay, situated on the northeast coast, is the largest fjord on the island and is characterized by two arms, East Bay and West Bay (Fig 1a, green square). Cumberland East Bay (EB) is approximately 15 km long and 3-5 km wide with a maximum depth of 270 m. Nordenskjöld Glacier terminates at the head of EB and there is a shallow inner basin with a prominent inner basin sill (Hodgson et al., 2014, Fig. 4). An outer basin sill, which is partially eroded near the center, marks the edge of the outer basin (Fig. 1c). Cumberland West Bay (WB) is approximately 18 km long and 2.5 - 5 km wide, with a maximum depth of 265 m. Neumayer Glacier terminates at the head of West Bay. The outer basin sill of WB is heavily eroded towards the southern half of the fjord (Hodgson et al., 2014). Bathymetric surveys have not extended close enough to the glacier to identify an inner basin sill (Hodgson et al., 2014), though chart data (Admiralty Chart 3588, Approaches to Stromness and Cumberland Bay) include shallow points (~30 m) extending the width of WB in the area highlighted in Fig. 1c (white dashed lines). We believe these data indicate a sill, and for the remainder of this paper, this is referred to as the 'postulated' inner sill.

Neumayer and Nordenskjöld Glaciers have shown markedly different rates of retreat over the past century (Cook et al., 2010; Gordon et al., 2008), with Neumayer Glacier retreating more than 10 km since 1955 and Nordenskjöld Glacier only ~2 km in the same time period. Cook et al. (2008) showed that the front position of Neumayer Glacier was relatively stable between 1955 and 1990, with the front in the vicinity of the postulated inner sill, but the mean rate of change in the front position increased rapidly between 1990 and 2008. It is not yet understood why these glaciers are showing such different rates of mass loss. However, plume dynamics and submarine melting may be key contributing factors, as studies of other high-latitude fjord systems have shown (Cowton et al., 2015; Motyka et al., 2017).

Previous work has demonstrated that an increase in submarine melting is a key driver of the observed increase in mass loss of tidewater glaciers in recent years, both directly through increased melt and indirectly by altering the ice front shape such that the rate of calving is increased (e.g., Luckman et al., 2015; O'Leary & Christoffersen, 2013). The melt rate is

approximately proportional to the difference between the temperature of the water and the ice freezing temperature (thermal driving) and the speed of the flow at the ice-ocean interface (boundary layer velocity) (Holland & Jenkins, 1999; Millgate et al., 2013). These quantities depend on the wider circulation regime within the fjord. Factors influencing the circulation regime include fjord-shelf exchange, atmospheric forcing, surface freshwater runoff, subglacial discharge, and fjord geometry, such as bathymetric sills (e.g., Bartholomaus et al., 2016; Boone et al., 2017; Catania et al., 2018; Cottier et al., 2010; Fraser & Inall, 2018; Hager et al., 2022; Mortensen et al., 2011). Fjord circulation patterns are complex and there is a lack of clear understanding of how the interactions between these processes lead to glacier retreat, particularly in fjord systems where warm water overlays colder water, such as in Cumberland Bay. This temperature structure is unusual for high-latitude fjords, which are generally characterized by cold, fresh waters from ice sheet runoff overlaying warmer waters (Lin et al., 2018; Silvano et al., 2017).

Oceanic melting of tidewater glaciers is enhanced when subglacial discharge meets the ocean and rises as a buoyant plume in contact with the submarine ice face (Slater et al., 2015). Subglacial discharge arises from surface glacial meltwater that has been directed through moulins and crevasses on the ice surface to reach the bed and then fed through a system of subglacial channels towards the glacier's grounding line, along with direct basal glacier melt (Chu, 2014). The discharge enters the ocean and entrains ambient ocean water generating inflow at depth as it rises as a buoyant plume in contact with the ice (Jenkins, 2011). The plume reaches either neutral density or the ocean surface, resulting in a thick flow away from the glacier. The inflow and outflow generated by the subglacial discharge is known as buoyancy-driven circulation (Carroll et al., 2015; Straneo & Cenedese, 2015). The interaction between buoyancy-driven circulation and submarine sills has the potential to alter the water circulation and the heat available for melting at the submarine face, as the sill acts as a barrier to ocean currents (Hager et al., 2022; Holland & Jenkins, 1999). This interaction may give rise to spatial differences in fjord systems with multiple glaciers and complex bathymetry and is likely to change with the seasonally varying rate of subglacial discharge (Bartholomaus et al., 2016).

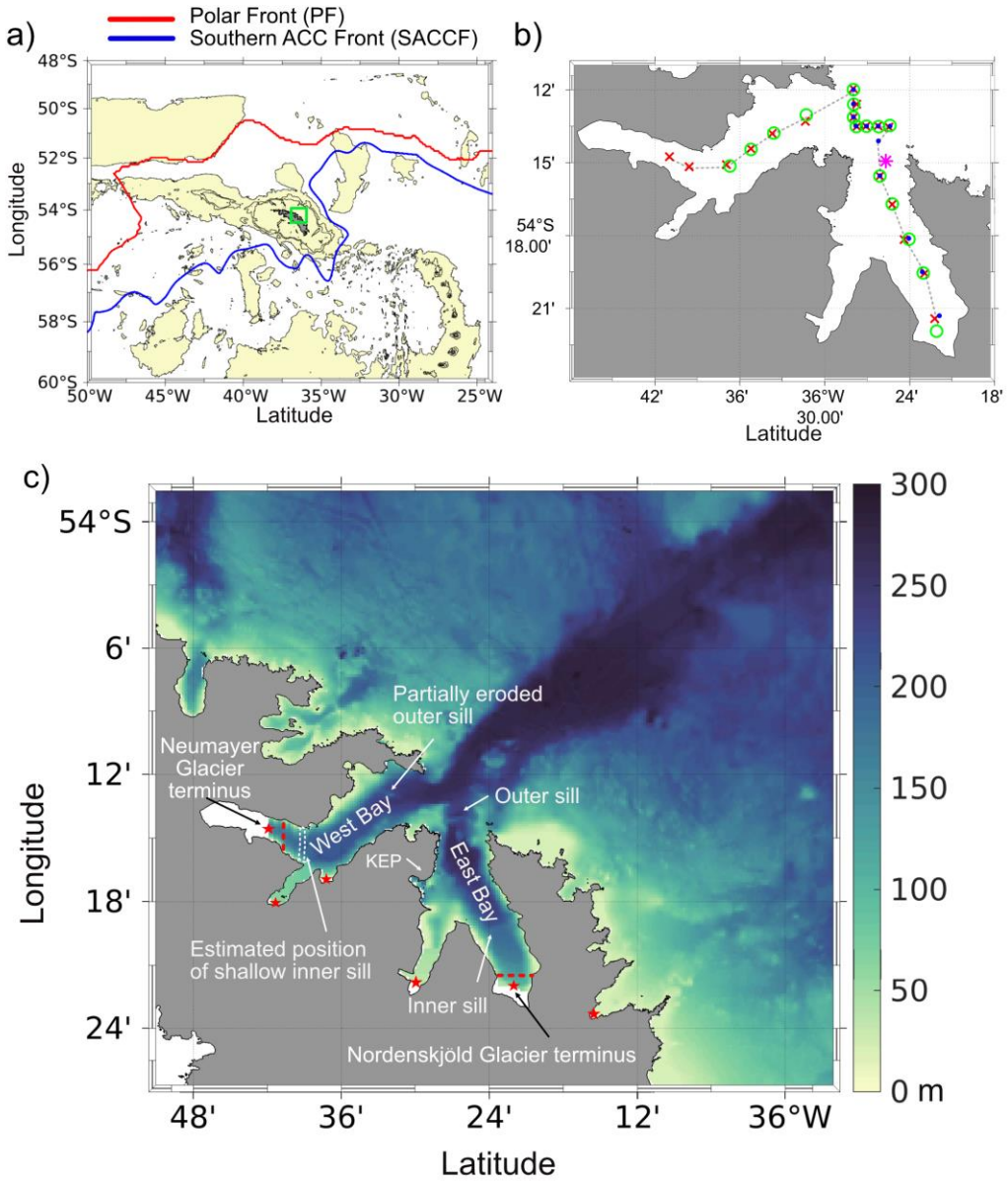

Figure 1. (a) Location of South Georgia in the Southern Ocean, with contours at 300, 1000, and 3000 m, and depths shallower than 3000 m shaded. Climatological locations of the Polar Front and Southern ACC Front are illustrated (Thorpe, 2001) and the location of Cumberland Bay is shown with the green square. (b) Positions of oceanographic surveys in Cumberland Bay from April 2012 (blue dots), February 2020 (green circles), November 2021 (red crosses), and January to November 2006 (pink star), and transect used for plotting data (grey dash line). (c) Cumberland Bay model domain, with bathymetry shaded (Hogg et al. 2016). Important bathymetric features are labelled, locations of glacier meltwater input are marked (red stars) and the locations of the cross-sections used for volume transport calculations are shown (red dashed lines).

132

In this study, we use oceanographic observations from Cumberland Bay and a new high-resolution ocean model (section 2) to address two main objectives. The first objective is to describe the seasonal and spatial variability between the two fjord arms, providing the first detailed study of this fjord system (section 3.1). The second objective is to identify key drivers of oceanographic variability that may influence glacier retreat, focussing on buoyancy-driven outflow and the presence of the postulated submarine sill (section 3.2). We then assess the limitations of the observations and modeling approach and discuss the implications of the results for understanding the rate of glacier retreat (section 4).

2 Data and methods

2.1 Observations

Four datasets of Conductivity Temperature Depth (CTD) data for Cumberland Bay from 2000 - 2021 were collated. These data provide information on the temporal and spatial variability of temperature and salinity in Cumberland Bay, as well as a resource for model validation. Firstly, CTD data were collected with irregular temporal frequency from five points in Cumberland East Bay between 2001 and 2006 by staff at King Edward Point station, using a Sea-Bird E19 (Fig 1b, pink star). Data from 2006 in the mouth of East Bay are chosen for analysis here, as this year and location had the best temporal coverage. Secondly, opportunistic CTD data were collected in Cumberland Bay on the 18th of April 2012 (JR272A) with a Sea-Bird E32 carousel water sampler (Fig. 1b, blue dots). Thirdly, between the 24th and 25th of February 2020 (DY113), a CTD survey was conducted with a Sea-Bird 9+ (Fig. 1b, red crosses). Finally, between the 9th and 14th of November 2021 (MV Pharos SG 12-21B) data were collected with a Valeport fastCTD (Fig. 1b, green circles). Data were processed by removing outliers, averaging into 2 m bins, and converting from in-situ temperature and practical salinity to conservative temperature and absolute salinity, respectively.

2.2 Oceanographic model

2.2.1 Model set up

A high-resolution Cumberland Bay model was built using the Nucleus for European Modeling of the Ocean version 4.0.6 (NEMO4), which solves the three-dimensional hydrostatic equations of motion for an incompressible fluid under the Boussinesq approximation on a structured computational grid. The vertical coordinate is represented with 35 vertical levels arranged as partial-cell z-levels. The levels are gradually stretched to achieve higher resolution in the surface layer, with a grid spacing near the surface of ~1 m reducing to ~30 m at depth. The domain is chosen to ensure the open boundaries are sufficiently far from the main region of interest (Cumberland Bay) to limit their influence, whilst allowing a good representation of variability in the wider shelf oceanography (Fig. 1c). Thus, the model domain extends to the shelf edge to the north, such that the maximum model depth does not exceed 300 m, and the western and eastern boundaries are positioned to capture a portion of the adjacent coastline (Young et al., 2014). A horizontal grid spacing of 1/500º latitude by 1/300º longitude (~200 m) is chosen with a resulting domain comprised of 280 by 240 grid cells in the horizontal. The resultant model is fine enough to resolve flows within Cumberland Bay whilst sufficiently computationally efficient for multi-year simulations.

NEMO4 uses the hydrostatic approximation, which saves considerably on computational expense. Although there are non-hydrostatic processes within the fjord, particularly over the sills, the effects are only likely to be resolved properly with a non-hydrostatic model if the horizontal grid spacing is significantly less than 100 m (Berntsen et al., 2009). However, a finer grid combined with the additional computational requirements of the non-hydrostatic solution would make the model too computationally expensive for multi-year simulations (Staalstrøm & Petter, 2016). A method for representing the subglacial plume using an offline model is described in section 2.2.4, which provides an efficient alternative for the representation of this non-hydrostatic process.

The model includes a free surface formulation and computational mode-splitting, with barotropic and baroclinic time steps of 1 s and 30 s, respectively. A free-slip lateral momentum boundary condition is used and the friction law at both the bathymetry and the ocean/atmosphere interface is assumed to be quadratic (non-linear) (Soontiens et al., 2016). A constant drag coefficient for surface and bed of 2.5×10^{-3} is chosen (Soontiens & Allen, 2017).

190 The Monotonic Upstream-centred Scheme for Conservation Laws (MUSCL) scheme is
191 used for tracer advection. The lateral diffusion scheme for tracers uses a rotated Laplacian
192 operator acting along iso-neutral surfaces. The lateral diffusive velocity and length scales are set
193 to 0.0009 ms^{-1} and 222 m respectively (Okubo, 1971). The lateral diffusion scheme for
194 momentum uses the bilaplacian operator acting in the horizontal (geopotential) direction with
195 lateral viscous velocity and length scales of 0.3 m s^{-1} and 222 m respectively. An energy and
196 enstrophy conserving scheme and the Hollingsworth correction are applied (Hollingsworth et al.,
197 1983; Penduff et al., 2007). The hydrostatic pressure gradient formulation is a Pressure Jacobian
198 scheme and the Generic Length Scale (GLS) scheme is used for the vertical turbulent mixing
199 (Umlauf & Burchard, 2003).

200 **2.2.2 Model bathymetry**

201 The model bathymetry was derived from a bathymetric dataset compiled by Hogg et al.
202 (2016) by averaging the 100 m resolution data onto the ~200 m grid (Fig. 1c). The main
203 bathymetric features - including the deep channels, shallow banks, and the coastal topography -
204 are mostly well captured at this resolution, with the exception that some small-scale features
205 (such as sills) are smoother than observed.

206 Official bathymetric data for the seabed exposed following the recent retreat of
207 Neumayer Glacier are not yet available. Shallow points in chart data and observed grounded
208 icebergs suggest a shallow inner sill exists, also hypothesized by Hodgson et al. (2014) and
209 referred to here as the 'postulated sill'. However, the width and depth of this potential sill are
210 unknown. Therefore, in the basic simulations, the choice was made to continue the known
211 shallow gradient of the bed topography towards the glacier terminus along the center of the fjord,
212 leading to a maximum depth of ~160 m adjacent to Neumayer Glacier. The adjacent data gaps
213 were filled by creating a quadratic 'U' shape across the fjord, assuming shallow coastal points of
214 20 m depth. This allows for an unrestricted channel for the simulated water flow. To consider the
215 impact of the postulated sill on the fjord oceanography, an artificial sill geometry was added for
216 a process test simulation. This was achieved by modifying the bathymetry such that it shallowed
217 steeply to 30 m across the width of the fjord, resulting in a bathymetric barrier one grid cell wide.
218 East Bay has more thorough coverage of observational bathymetry data, including close to
219 Nordenskjöld Glacier terminus, with a maximum depth of ~70 m adjacent to the glacier. A few

individual grid cells were altered to allow a gentle shallowing towards coastal edges of the fjord directly adjacent to the glacier and to give a smoother horizontal glacier terminus shape to aid model stability.

2.2.3 Open and surface boundary forcing

The model is forced at the open boundaries with tides from a global tidal model (TPXO9.2; (Egbert & Erofeeva, 2002) using eight tidal constituents (Q1, O1, P1, K1, N2, M2, S2, K2) and with 3D flows, sea surface height, temperature, and salinity derived from a regional South Georgia model (Young et al., 2016). Forcing data from the regional model are bilinearly interpolated to the open boundary points. The barotropic open boundary forcing uses the Flather Radiation Scheme (Flather, 1994). The baroclinic flows are treated with the 'zerograd' (Neumann) scheme where the values at the boundary are duplicated with no gradient. Tracers at the boundary use the Flow Relaxation Scheme which applies a simple relaxation of the model fields specified at the open boundary over a zone of 9 grid cells (Davies, 1976; Engedahl, 1995).

Surface boundary forcing is derived from the ERA5 reanalysis dataset with 30 km horizontal grid resolution (Hersbach et al., 2020). A bulk formulation (NCAR, Large & Yeager, 2004) is used. Interpolation of the coarse atmospheric forcing to the fine grid spacing of the model is achieved using the ‘on-the-fly’ option in NEMO4 and supplying a weights file for bilinear interpolation.

2.2.4 Terrestrial freshwater forcing

The freshwater contributions of surface run-off and sub-glacial outflow in the domain are taken from a theoretical climatological annual cycle calculated from historical precipitation data, glacier basin size, and positive degree days (Young et al., 2011). The freshwater flux for each glacier is injected into the appropriate ocean cell adjacent to the glacier and distributed over a prescribed depth range; the locations of glaciers contributing meltwater to the model are shown in Fig. 1c (red stars). For the two large marine-terminating glaciers in Cumberland Bay, the choice of depth range required consideration of subglacial meltwater plume-driven dynamics. Based on knowledge from other high-latitude ice masses, it is assumed that a majority of surface meltwater from the glaciers descends through crevasses and moulins and enters subglacial channel systems at the bed (Chu, 2014). These channels meet the ocean at the grounding line of the marine-terminating glaciers at the fjord head, leading to the rise of subglacial discharge as a

buoyant plume (Hewitt, 2020). The theoretical meltwater cycle is thus split into 10% surface runoff and 90% subglacial discharge. Given the uneven bathymetry, for the purposes of this modeling study it was assumed that 'localized channels' are formed, which emerge at the deepest part of the glacier termini over a width of one grid cell (~200 m) (Slater et al., 2015). In practice, buoyant plumes tend to rise in contact with the submarine ice face, causing melt and continue to entrain ambient ocean water until they reach neutral buoyancy (or the surface) where they intrude horizontally into the ocean (Hewitt, 2020; Sciascia et al., 2013). As NEMO4 uses the hydrostatic assumption, it is not possible to resolve the plume dynamics within the model, and so a parameterization is required.

The default option for meltwater runoff in NEMO4 is to introduce fresh, cold meltwater into the surface layers of the model, extending down to a specified depth. However, this does not capture potentially important increased buoyancy-driven outflow as a result of subglacial discharge, and could alter the ocean stratification unrealistically (Cottier et al., 2010). A new improvement has been developed for this study that adapts the freshwater input by incorporating the subglacial plume characteristics according to an offline plume model. This offline model requires ocean conditions, which necessitates an iterative process, as follows.

First, the model is run for 10 years (following a year spin-up) with no terrestrial freshwater forcing. The deepest ocean grid cell column adjacent to the glacier is identified as the point to which the subglacial discharge would be directed via the hydraulic gradient. Next, an offline plume model is run that calculates the properties of the plume based on Slater et al. (2017; equations 4a – 4d) and the melt rate of the submarine ice face, based on Jenkins (2011; equations 7 – 9). The plume model uses the temperature and salinity from the previously identified model grid cell column and the theoretical daily subglacial discharge, Q_S (Fig. 2a). Assuming values for the plume model constants following Slater et al., (2017), the model is solved for the temperature (T), salinity (S), volume (Q_P) and depth (D) at which the plume reaches neutral buoyancy (termination depth) (Fig. 2 b-e). Finally, the meltwater properties are set to the plume T and S and inserted into the relevant NEMO grid cell from the surface down to 10 m, or down to the termination depth D if the plume terminates below the surface. It is not currently possible to simulate a wholly subsurface plume in NEMO4. The surface freshwater runoff (the remaining 10% of the theoretical daily meltwater) is inserted into an adjacent grid cell to that used for the plume model, to simulate the portion that would remain on the surface of

281 the glacier running off from supraglacial streams. From here on, the meltwater-laced plume
282 outflow is referred to as the WB-PLUME or the EB-PLUME, which consists of >95 % seawater
283 (Fig 2. a, d).

284 The new freshwater parameterization provides a representation of glacier plume and
285 buoyancy-driven outflow within the limitations of the NEMO framework, which is not captured
286 by adding fresh, cold meltwater into the surface alone. However, entrainment of ocean waters
287 into the plume at depth is not included in NEMO, which is therefore not capturing the extent of a
288 thick, but slow inflow below the plume's neutral buoyancy (Mortensen et al., 2011). The ambient
289 ocean properties used to calculate the plume are also not coupled to the resulting plume. These
290 limitations of the modeling approach are considered in the discussion.

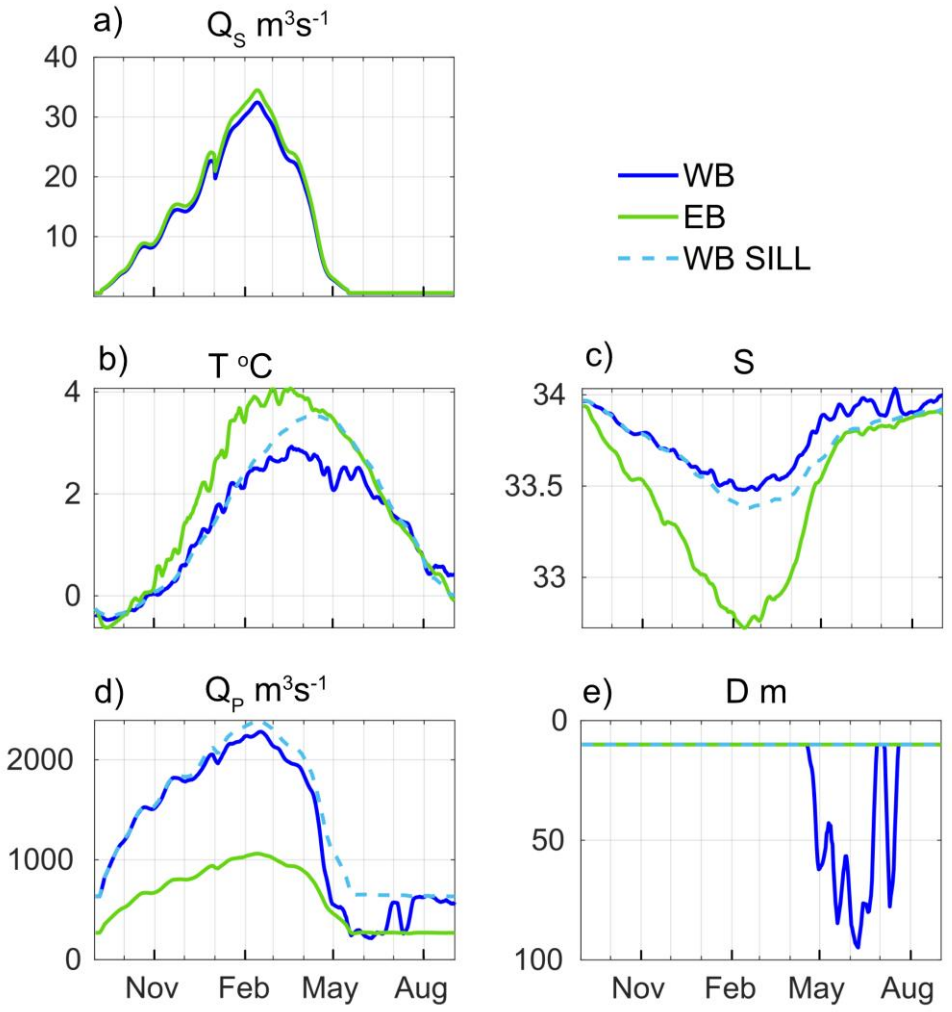

291

Figure 2. (a) The theoretical climatological cycle of meltwater discharge, Q_1, for Neumayer Glacier in WB (blue) and Nordenskjöld Glacier in EB (green) September 2005 to August 2006 (Young et al. 2011). (b) Conservative temperature, T, (c) absolute salinity, S, (d) volume, Q_2, and (e) termination depth, D, for WB-PLUME (blue) and EB-PLUME (green) in the baseline PLUME run and the for the WB-PLUME in the SILL-PLUME run (dashed blue) September 2005 to August 2006.

2.3 Model validation and run configurations

The model was validated using 11 months of CTD data collected in 2006 from the mouth of East Bay (Fig. 1b, pink star). The closest point to the mid-depth of each model level was taken from the observational data to allow direct quantitative comparison. The Root Mean Squared Error (RMSE) for conservative temperature and absolute salinity was calculated for each month of 2006 (excluding December when data were not collected) as well as the total RMSE (TRMSE). The mean near-surface error (MSE) (average of each point in the top 10 m) and mean near-bed error (MBE) (bottom model level) were calculated by subtracting observational data from model data. Finally, the Cost Function (CF) was calculated, which is a measure of model predictive skill that incorporates the standard deviation of the observational data (Holt et al., 2005). The results (Table 1) suggest that the model reproduces the observed temperature very well with the CF value well below 1 at this location. Although the CF for salinity is over 1, likely due to the timing of freshwater input (see section 3.1.1), the TRMSE is relatively small, demonstrating that this model is a useful tool for exploring the drivers of spatial and temporal variability.

	TRMSE	**MSE**	**MBE**	**CF**
T	0.39 ^{o}C	-0.04 ^{o}C	-0.24 ^{o}C	0.09
S	0.19 g/kg	-0.02 g/kg	0.01 g/kg	1.19

Table 1. Results of statistical tests from model validation.

The model is initially run from 1999-2000 to allow spin-up from initial conditions interpolated from an existing regional model (Young et al., 2016). Then the full model is run for 2000 – 2012, without the postulated sill. Process tests, which test the sensitivity of the system to individual factors, are run for September 2005 to August 2006. The baseline scenario is referred to as PLUME and the test removing WB-PLUME and EB-PLUME is referred to as NOPLUME. Inserting the shallow sill in WB and recalculating WB-PLUME and EB-PLUME via the same method as the baseline is referred to as SILL-PLUME. Inserting the sill without the WB-PLUME and EB-PLUME is referred to as SILL-NOPLUME.

3 Results

3.1 Seasonal and spatial variability

3.1.1 Temperature and salinity

The time series from the point source CTD data in 2006 reveals a strong seasonal cycle in conservative temperature (T) and absolute salinity (S) (Fig. 3). The water column is stratified in austral summer and early autumn, with the warmest surface waters between February and April due to surface heating, reaching a maximum of 4.1 ^{o}C in March, and with temperatures decreasing with depth. The water column cools in autumn and winter to a minimum of 0 ^{o}C by surface cooling and the water column is well mixed between August and October (Fig. 3a) due to mixing from winter storms. A fresh near-surface lens is observed between March and July with a minimum salinity near-surface of 32.9 in April. This is likely a combination of precipitation or the melting of floating ice, due to being a significant distance from the glaciers. Salinity increases with depth, with the greatest salinity of 34.3 near-bed between January and June, characteristic of inflowing dense shelf waters. Modeled temperature and salinity for the same location and year are largely consistent with the CTD data (Fig. 3b). The most significant difference in temperature is that the model predicts temperatures below zero (Fig. 3b). The timing of the seasonal salinity cycle is less consistent with the CTD data, with the fresh surface layer predicted ~2 months earlier than observed (Fig. 3). This may be because the theoretical melt cycle does not consider a time delay between surface heating and coastal fluxes of freshwater. In addition, as it is a climatology, it does not include the atmospheric conditions specific to 2006.

The CTD transect data from WB and EB provide some spatial context for the seasonal cycle. Hereafter, the seasonal cycle is described from spring (September) through to winter (August) and the transect CTD data from 2012, 2020, and 2021 are ordered according to season rather than year (Fig. 4). For each survey, the transect plots start from the CTD cast closest to Neumayer Glacier in West Bay and end close to Nordenskjöld Glacier in East Bay (Fig. 1b dashed grey line), with distance along the transect referenced to the central point between WB and EB mouths. In November (late spring), the warmest surface waters are at the fjord mouths and close to Neumayer Glacier (Fig. 4a). Isotherms show a complex structure, generally deepening toward the fjord mouths. Near-bed waters are slightly warmer near the mouth of

345

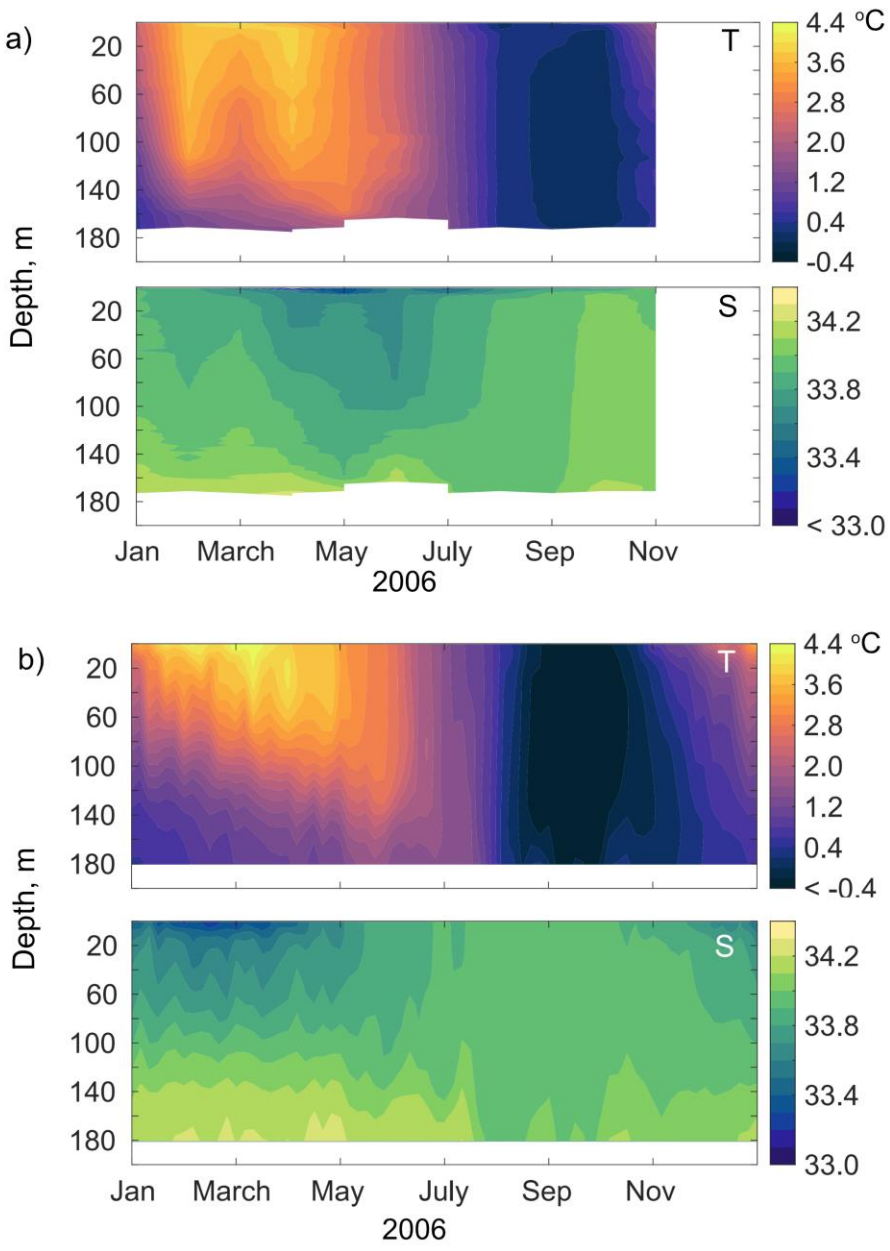

Figure 3. Conservative temperature (T) and absolute salinity (S) from (a) the CTD survey taken in the mouth of East Bay (Figure 1b, pink star) for each month, excluding December, in 2006, and (b) from the equivalent model location for each 5-day mean January to December 2006.

346

347

EB. A thin near-surface fresh lens extends along the length of WB and near Nordenskjöld Glacier in EB. Isohalines deepen steeply close to both glaciers and toward the fjord mouths. In February (late summer), there is a cold surface layer close to both Neumayer Glacier and Nordenskjöld Glacier, notably colder in WB. Below a subsurface warm layer at ~20 m, temperature decreases with depth and isotherms shallow gently toward the glaciers. Near-bed temperatures are slightly higher across the fjord mouths. The fresh surface lens observed in spring is again evident in summer, though fresher and deeper. In April (autumn), the upper ~100 m is more mixed and cooler. A thin fresh surface lens is again apparent, weaker than summer and more constrained spatially to WB mouth, and mid-way along EB.

The transects indicate that glacier processes may modify the water properties at the head of each fjord arm through cooling and freshening, particularly in summer. Near the fjord mouth, shelf-fjord exchange processes increase salinity at depth, and in spring and summer result in a near-bed intrusion of slightly warmer water. In February, the water mass properties below 25 m are very similar along the entire transect but surface waters are notably colder and fresher in WB (Fig. 5). The Temperature-Salinity (TS) lines for WB (Fig. 5, red lines) show the signature of melted glacial ice mixing with seawater; above 25 m, the lines approximately follow a melt line (grey line Fig. 5), which has a slope of roughly 2.5 ^{o}C per salinity unit (Gade slope, Gade, 1979; Mortensen et al., 2013; Straneo & Cenedese, 2015). This signature of melt could be both due to the direct melting of the submarine ice face and the submarine melting of icebergs. The change in the slope of the TS lines closer to the surface suggests that these waters are modified by a mixture of submarine melt, subglacial discharge, and surface melt, as they lie between the melt and runoff lines (Straneo & Cenedese, 2015).

The hydrographic data reveal some spatial differences between WB and EB. However, the CTD surveys do not extend close enough to Neumayer Glacier terminus to detect important differences in the glacier adjacent water column properties, and there are no data on the ocean currents. Further investigation requires analysis of the regional high-resolution ocean model.

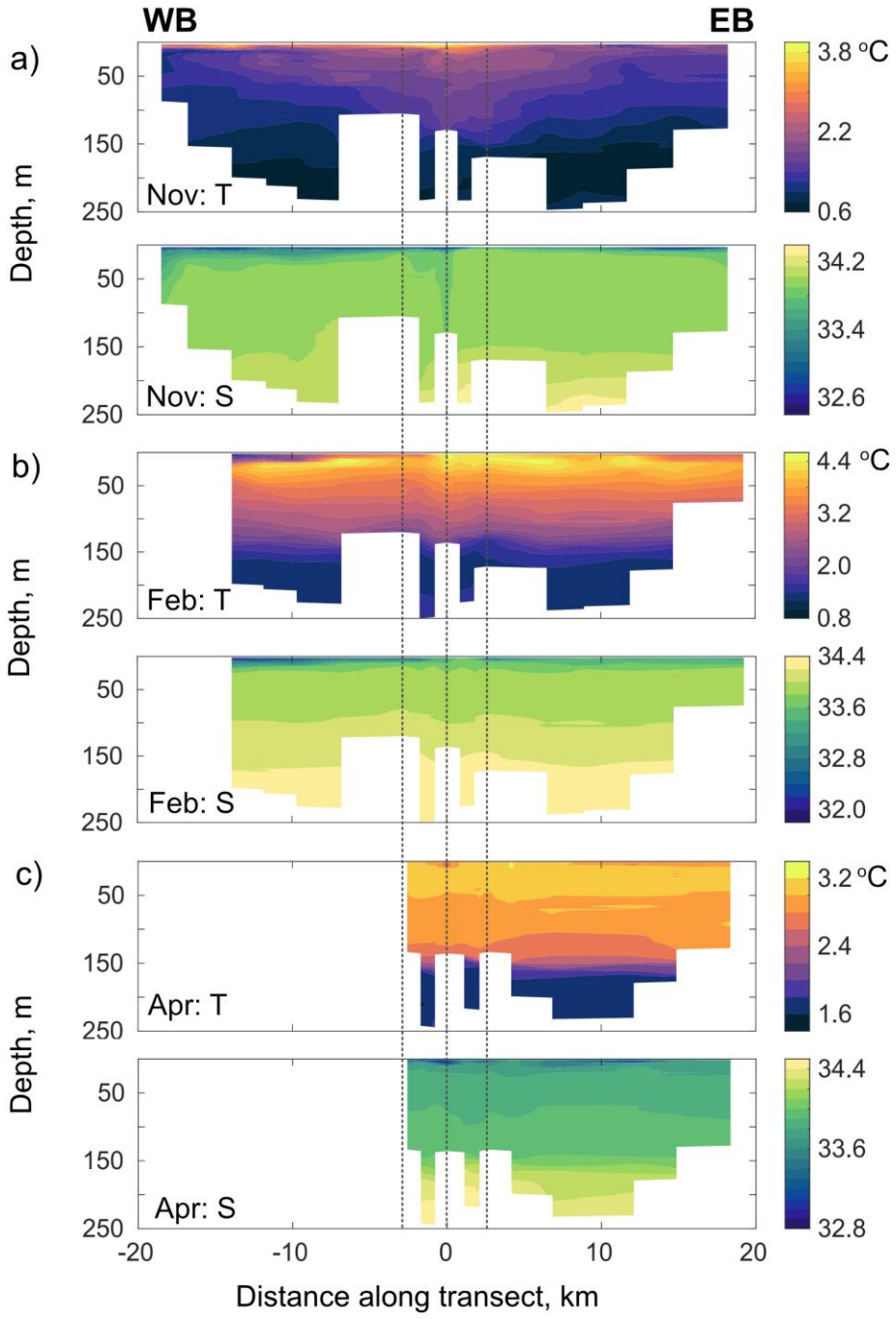

Figure 4. Transects (WB to EB; grey dashed line in Fig. 1b) of conservative temperature (T) and absolute salinity (S) for CTD surveys from (a) November 2021, (b) February 2020 and (c) April 2012. Black dashed lines indicate where the cross-mouth transects start and end. Note, the color bar scales are different for each month.

374

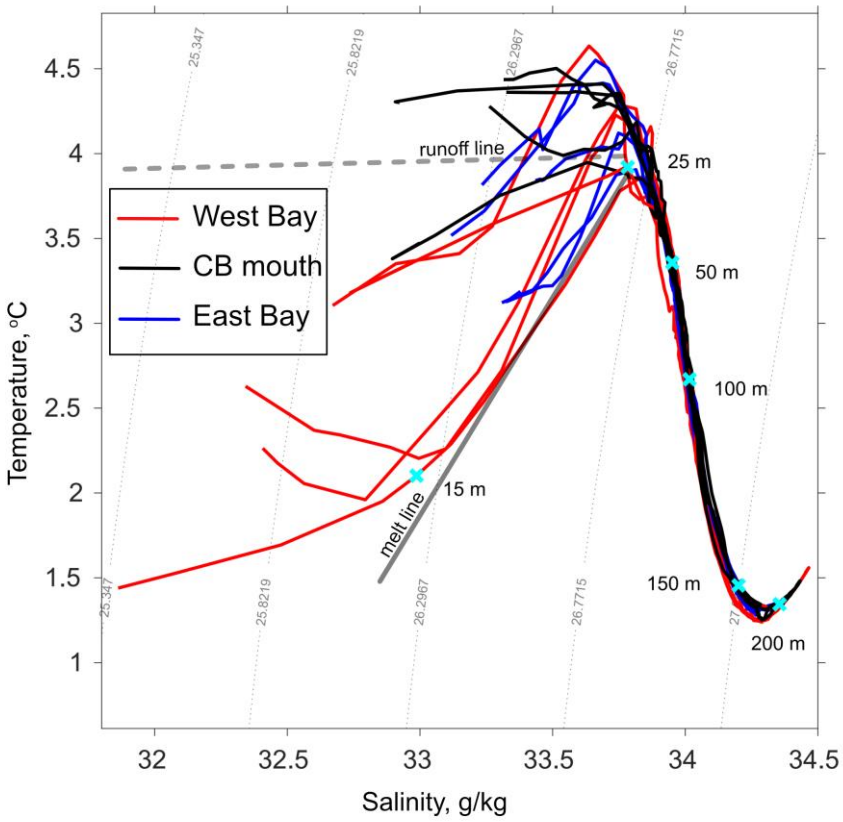

Figure 5. Temperature – salinity diagram for each CTD cast in February 2020, separated by color into West Bay transect (red), cross-mouth transect (black) and East Bay transect (blue). Isopycnals (kg/m – 1000, dotted curves), melt line (solid grey) and runoff line (dashed grey) are also shown.

3.1.2 Flow fields and sea surface temperature

A more detailed description of spatial and temporal oceanographic variability in Cumberland Bay can be gained from analysis of high-resolution model output, here focusing on near-surface flows, depth-averaged flows and sea surface temperatures (SST) (Fig. 6). The seasonal variability is illustrated with monthly averages for November (spring), February (summer), May (autumn), and August (winter).

The surface (top model layer) currents show largely the same pattern as the depth-averaged currents for each month (Fig. 6). In spring and summer there is enhanced flow along the north coast of WB and the east coast of EB which crosses to the west coast at the mouth, and is subsequently entrained into the stronger northwestward shelf flows (Fig. 6). The Rossby radius of deformation is larger than the narrow fjord width, so cross-fjord variations are not induced by the Coriolis force (Cottier et al., 2010). The baroclinic surface flows are strongest in summer when the volume of meltwater runoff, and therefore buoyancy-driven outflow, is greatest (Fig. 2a) which is inferred by the greatest difference between the surface and depth-averaged flows (Fig. 6). Surface flows weaken in May, as meltwater runoff reduces steeply (Fig. 2a). Winter storms drive mixing which weakens the stratification allowing bathymetric steering of coastal flows into the fjord mouth. The buoyancy-driven outflow is no longer the dominant driver of circulation in winter, reflecting the seasonality of freshwater forcing.

The sea surface temperature (SST) is cold in spring (~0 ^{o}C), coldest in the tributary fjords and at the head of WB (Fig. 6). The SST warms significantly in summer and autumn (~3-4 ^{o}C) though notably colder in WB compared to EB. The colder surface waters in WB are consistent with the colder properties of WB-PLUME compared to EB-PLUME (Fig. 2b). In winter, the SST is similar between the fjord arms, consistent with the lower volume of the WB- and EB-PLUME and buoyancy-driven outflow no longer being a dominant driver of circulation.

While many aspects of seasonal variability are not yet verified, the model provides a useful tool for testing hypotheses. Variability in shelf-fjord exchange, apparent in the flow fields and near-bed water properties, and the interaction of such flows with the fjord outer sills, will contribute to temporal and spatial variability at the fjord mouths, however, this is beyond the scope of the present study. Instead, based on the clear influence of glacial meltwater in the observations, we focus on the role of buoyancy-driven outflow in driving spatial and temporal

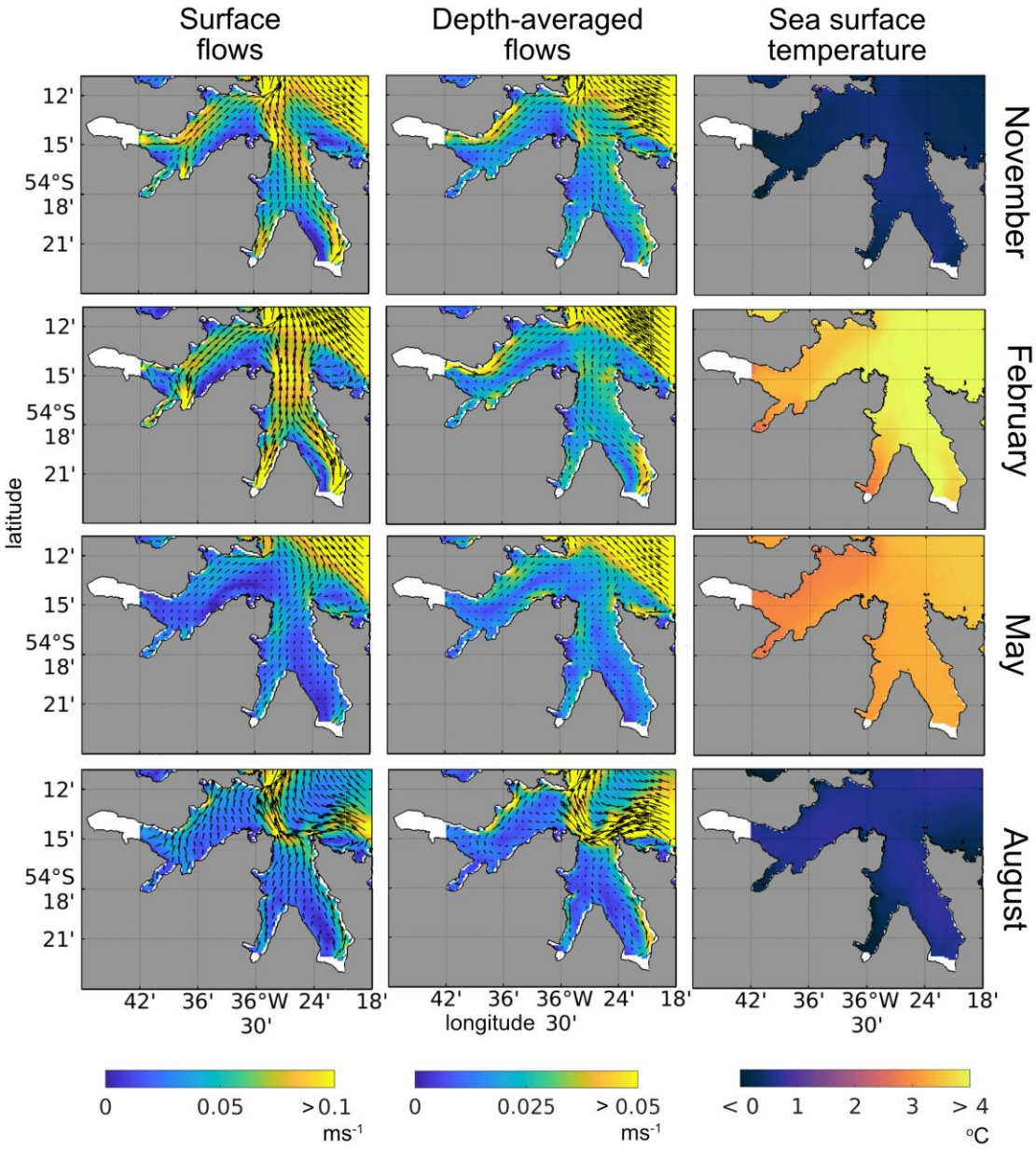

409

Figure 6. Surface flow, depth-averaged flow, and sea surface temperature, averaged over the months of November, February, May, and August. Note the difference in color scale between the surface and depth-averaged flows.

variability close to Neumayer and Nordenskjöld Glaciers and we concentrate further model analyses on this region.

3.2 Drivers of variability

3.2.1 Buoyancy-driven outflow

Volume transport through cross-sections ~1 km from Neumayer and Nordenskjöld Glaciers show a distinct difference in circulation patterns between the two fjord arms (Fig. 7, locations of cross-sections in Fig. 1c, red dashes). In WB, the average volume transport in November shows a 4-layer structure from the surface to the bed of alternating outflow and inflow. In February, when the volume of WB-PLUME is greatest (Fig. 2d), there is strong outflow in the north, with weaker inflow in the south in the upper ~60 m. The outflow in the north becomes a subsurface feature in May with surface inflow across the width of WB; this coincides with a sharp reduction in WB-PLUME volume and the onset of subsurface WB-PLUME termination (Fig. 2e). In August, following a period of low WB-PLUME volume, the structure reduces to 2 layers with surface outflow and inflow below ~50 m. In November in EB, there is a predominant 2-layer structure of surface inflow and outflow at depth in the west, with the reverse structure in the east (Fig. 7b). This pattern continues largely unchanged in February and May, before a distinct shift in August to inflow in the west and outflow in the east (Fig. 7b), due to more barotropic flows in the destratified water column (Fig. 3). The EB-PLUME is confined to the upper 20 m, increasing the strength of the surface outflow in spring and summer in line with the near-surface flows (Fig. 6).

To test the influence of the WB- and EB-PLUME on the circulation patterns, we compare directly to the NOPLUME scenario. The total volume transport through each section was integrated across the fjord width and averaged over 30-day intervals to enable visualization of the seasonal cycle in transport variability with and without the plume (Fig. 8). In WB, the thick surface outflow that moves subsurface between April and July is clearly a response to the WB-PLUME; with NOPLUME there is a thin surface outflow and subsurface inflow between ~10 and 50 m throughout the year (Fig. 8a). In EB, outflow is confined to the upper ~20 m for the majority of the year with EB-PLUME, becoming thicker and weaker in winter. With NOPLUME the transport pattern remains the same, but with weaker surface outflow (Fig. 8b).

440

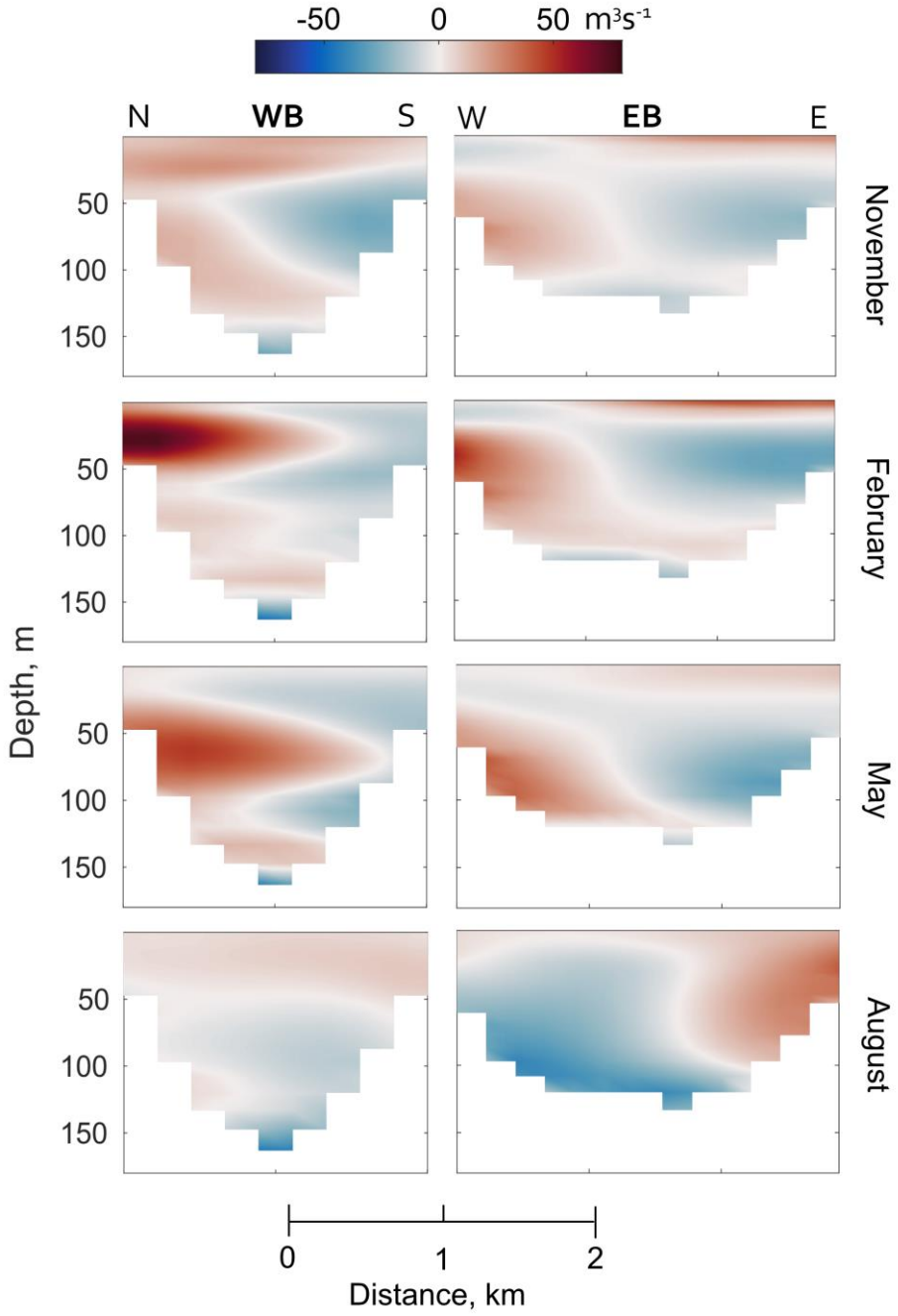

Figure 7. Monthly-averaged volume transport through cross-sections ~1 km from Neumayer Glacier (WB, north (N) to south (S)) and Nordenskjöld Glacier (EB, west (W) to east (E)) (Fig. 1c, red dashed lines). Red indicates outflow, toward the fjord mouth, and blue indicates inflow, toward the glaciers.

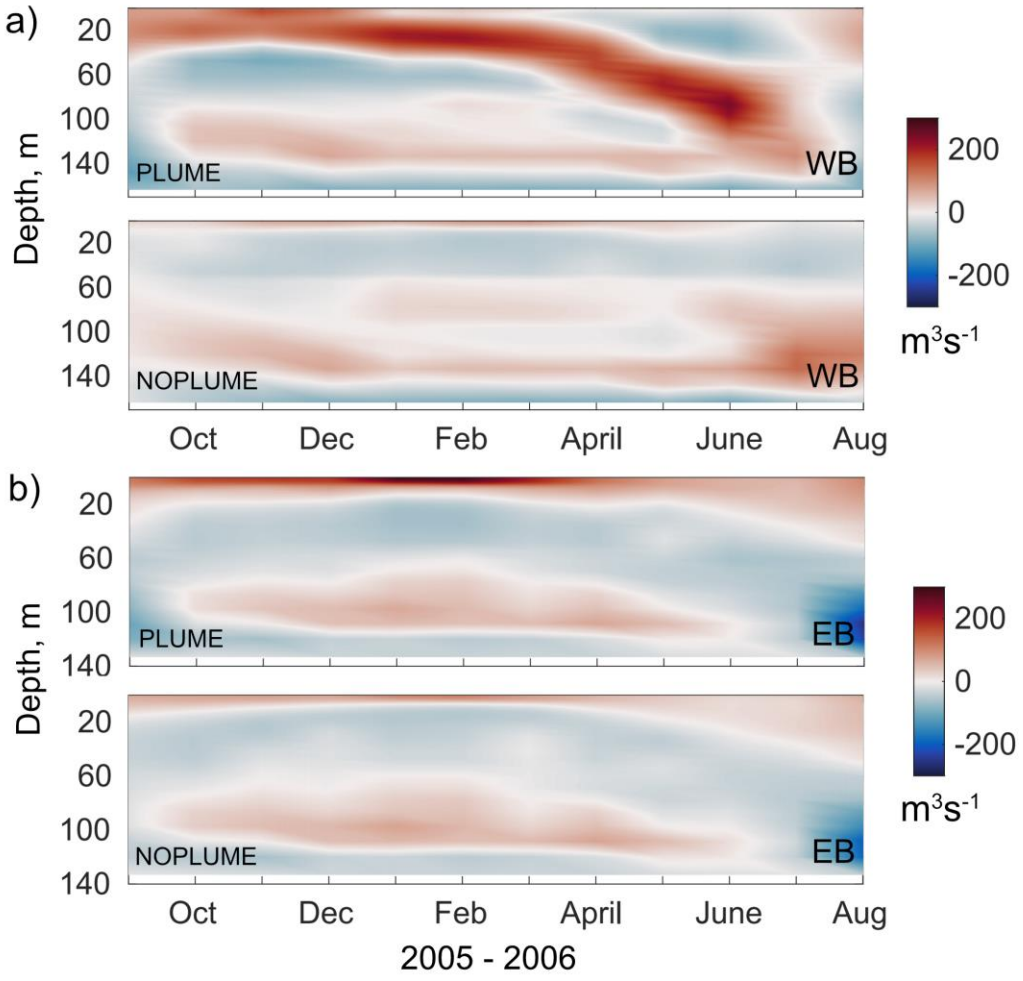

441

Figure 8. Monthly-averaged volume transport integrated across model levels through cross-sections ~1 km from (a) Neumayer Glacier (WB) and (b) Nordenskjold Glacier (EB) (red dashed lines in Fig. 1c), comparing PLUME and NOPLUME model runs; September 2005 to August 2006.

442

443

444 The buoyancy-driven outflow from WB-PLUME and EB-PLUME drive distinctly
445 different circulation patterns for much of the year (Fig. 8). One key difference between WB and
446 EB underlying this disparity is the seabed depth adjacent to the glaciers. WB is deeper, hence the
447 water properties used to calculate WB-PLUME are colder and more saline relative to those in
448 EB (Fig. 2) and this is reflected in the SST (Fig. 6). The outflow of WB-PLUME is greater and
449 spread over a larger depth in WB compared to EB. Due to the volume of subglacial discharge
450 and the properties of the water in autumn, the plume in WB terminates below the surface, driving
451 a different circulation pattern at this time of year (Fig. 7). These results strongly suggest the
452 subglacial plume is an important feature, and the plume dynamics are sensitive to the relatively
453 small depth range of these shallow glaciers. The model simulations demonstrate that the glacial
454 plumes have a significant impact on patterns of circulation in WB and EB, and it is possible the
455 retreat rates of Neumayer and Nordenskjöld Glacier are sensitive to the small differences in
456 oceanography. However, a perhaps more significant driver of spatial differences in
457 oceanography is the postulated inner sill in WB.

458 **3.2.2 West Bay postulated inner sill**

459 The model simulation was repeated with an inner sill artificially inserted in WB as barrier
460 1-grid cell wide and sitting at 30 m below the sea surface (Fig. 9a, location in Fig. 1c white
461 dashed line) (SILL-PLUME) to test the impact of the postulated WB inner sill on the
462 oceanography. Analysis of water properties in April for a transect along the center of WB shows
463 the new inner basin to be warmer, fresher, and well-mixed compared to the outer basin (Fig. 9a).
464 The near-bed temperature in the center of the inner basin is ~2 ^{o}C higher than the comparable
465 PLUME run (Fig. 9b). Higher near-bed temperatures are also predicted by the SILL-NOPLUME
466 simulation (Fig. 9b), which shows that the sill is the underlying driver in both cases. Warmer,
467 fresher surface waters from the outer basin flow over the sill, where they are mixed, while deeper
468 waters are blocked by the sill, leading to near uniform T and S in the inner basin (Fig. 9a),
469 similar to observed processes over transverse ridges on the West Antarctic Peninsula shelf
470 (Venables et al., 2017). With no sill present, WB-PLUME decreases the near-surface
471 temperature in summer and autumn (Fig. 9b, blue lines). For the SILL-PLUME scenario, WB-
472 PLUME decreases the near-surface temperature in summer and slightly increases the near-
473 surface temperature in autumn (Fig. 9b, red lines). Therefore, the presence of the sill affects the

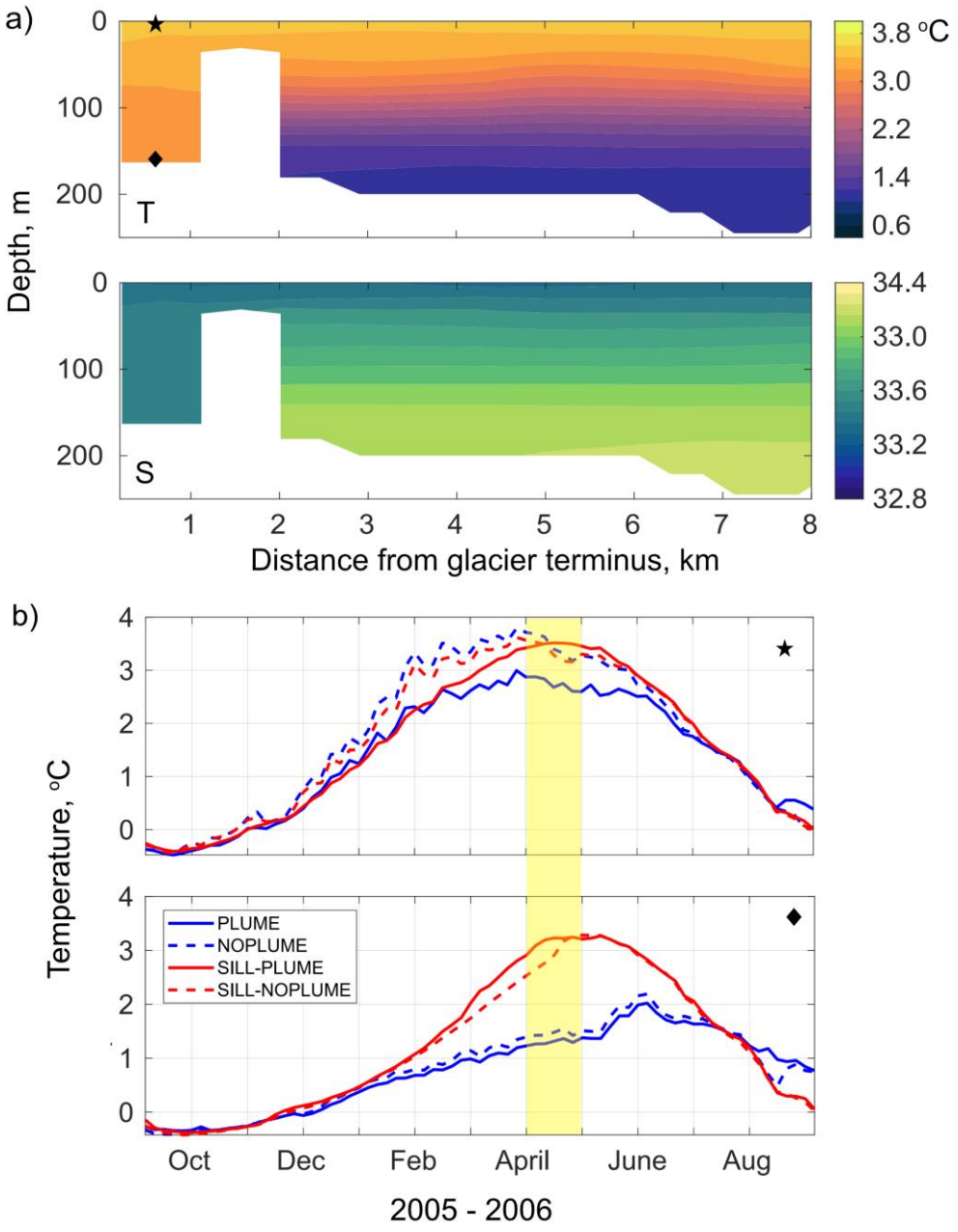

Figure 9. (a) Monthly averaged (April 2006) conservative temperature (T) and absolute salinity (S) from the SILL-PLUME model run for an 8 km transect along the centre of WB from Neumayer Glacier terminus. (b) 5-day mean near-surface (star in panel (a)) and near-bed (diamond in panel (a)) temperatures for September 2005 to August 2006, from the four model runs defined in the legend. The month of April is highlighted in yellow.

full water column near the glacier, but the most significant changes are near-bed with the increase in temperature, which may have implications for glacier retreat.

The integrated volume transport through the WB section was calculated for the SILL-PLUME and SILL-NOPLUME simulations for comparison with the results described in section 3.3. The transport patterns through the section, which now lies within the inner basin, show that when a sill is present the buoyancy-driven outflow drives a different circulation pattern (Fig. 10). The SILL-PLUME simulation predicts a thick surface outflow throughout the year in the upper ~50 m, deepening in winter, and inflow between ~50 and 100 m from spring to early autumn. Below ~100 m there is relatively low volume transport in spring and summer, and a strong inflow in autumn and winter. Compared with the SILL-NOPLUME run, it is apparent that the WB-PLUME is driving the pattern of strong outflow overlying inflow in spring and summer, and extending the duration of near-bed inflow in autumn and winter. As the peak of the sill is 30 m below the sea surface, a portion of the buoyancy-driven outflow flows over the sill, but below 30 m the outflow is blocked by the sill and re-circulates as subsurface inflow. Warmer surface waters from the outer basin flow into the inner basin over the sill along the south coast in the spring and summer (not shown), but integrating the volume transport along model levels masks this cross-fjord variability as the outflow from the plume dominates. In winter, as the volume of the WB-PLUME lessens and the density in the outer basin increases (temperatures cool and salinity increases, Fig. 3), waters from the outer basin encroach into the inner basin, sink, and present as a strong inflow at depth (Fig. 10).

An important difference between the model runs with and without an inner sill is that the PLUME run no longer has a sub-surface terminating plume for a portion of the year in WB (Fig. 2e). Due to the now uniform density within the inner basin resulting from the sill, the plume, derived from SILL-NOPLUME, does not reach any neutral density before the surface at any time of the year.

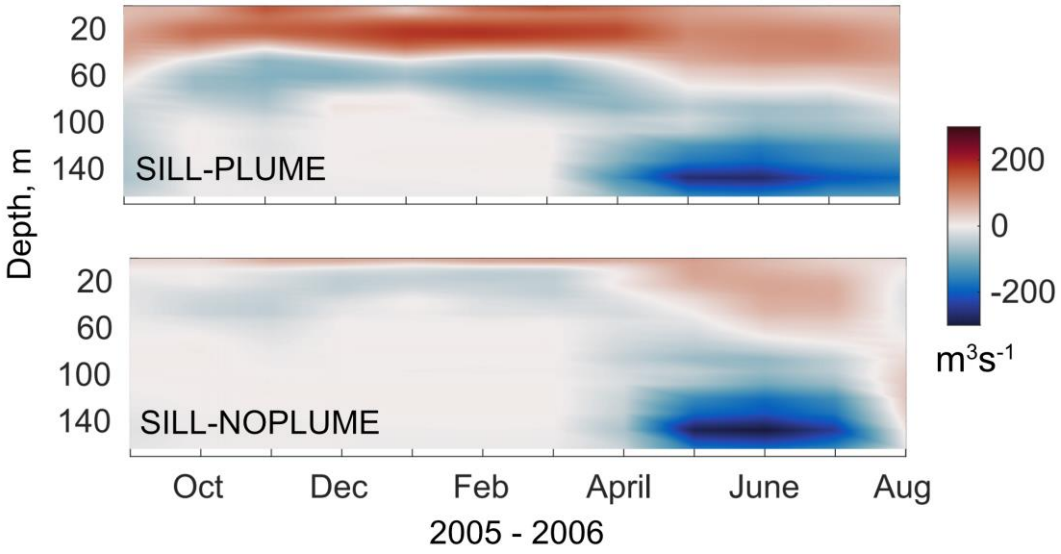

Figure 10. Monthly averaged volume transport integrated across model levels though the cross-section in WB (red dashed line Fig. 1c) for the SILL-PLUME and SILL-NOPLUME model runs; September 2005 to August 2006 Red indicates transport toward the fjord mouth, and blue indicates transport toward the Neumayer Glacier terminus.

4 Discussion

4.1 Oceanographic variability and modeling limitations

The oceanographic data presented and analysed in this study provide valuable information on the hydrography of Cumberland Bay. Freshwater signals are apparent in the data, but whether this can be attributed to surface meltwater runoff, subglacial discharge, melting of ice mélange, or increased precipitation is not completely clear. The cold, fresh signature of meltwater emerging as subglacial discharge may not be retained due to plume entrainment, meaning this can be hard to identify in the CTD data (Carroll et al., 2015). The oceanographic data reveal a strong seasonal cycle likely due to the combined effects of freshwater forcing,

shelf-fjord exchange, and atmospheric forcing (particularly winds). However, the temporal and spatial limitations of the observational data hinder a more detailed analysis.

With the use of the new high-resolution oceanographic model, we identified that freshwater forcing, which is dominated by subglacial discharge at the two main glaciers at the heads of WB and EB, is a key driver of spatial variability in spring through to autumn. This is due to the seasonal cycle of subglacial meltwater input and the bathymetric differences between the fjord arms. Wind forcing and fjord-shelf exchange likely dominates the spatial variability in flows in winter and are the focus of ongoing research.

The addition of an inner sill in WB has a significant impact on the simulated seasonal and spatial variability and has implications for the retreat of Neumayer Glacier, discussed further below. Neither scenario can yet be considered a more accurate representation of WB as the true bathymetry and the extent of the sill are unknown. However, the results clearly identify the sensitivity of the fjord oceanography to bathymetry and geometric controls on the circulation regime and suggest that buoyancy-driven circulation is likely to have varied considerably at different stages of past glacier front positions.

Though the model provides useful insights, the caveats must be considered. It is stressed that the plume dynamics and ocean model are not coupled, which limits the interpretation of the results. The ambient water column entrained in the offline plume model is unmodified by freshwater forcing, and the circulation resulting from entrainment into the plume is not captured, suggesting the ocean model may be underrepresenting inflow at depth. The implications of this are difficult to infer without the use of a coupled model. Additionally, the melting of icebergs is not represented in the model but is likely to have some influence on the hydrography (Fig. 5) and circulation (Davison et al., 2020). Despite these limitations, this study provides valuable insights into the oceanographic variability in Cumberland Bay, while emphasizing the importance of representing plume dynamics for the simulation of circulation in fjords with marine-terminating glaciers.

4.2 Implications for glacier retreat

Neumayer Glacier in WB has retreated far quicker than Nordenskjöld Glacier in EB but the drivers of this differential retreat rate are currently unknown. We hypothesize here that

changes to water column properties adjacent to Neumayer Glacier due to a postulated shallow inner sill in WB are playing a key role in the differential retreat rate.

The results of model experiments show that the presence of a bathymetric barrier representing the inner sill blocks colder waters at depth, resulting in a warmer, well-mixed inner basin (Fig. 9a). This warmer water in the vicinity of the glacier terminus can be inferred to increase glacier melt, and even potentially drive a positive feedback mechanism that would further increase glacial retreat from the sill, although as there is no ice-plume-ocean coupling in the model, such implications remain speculative. Assuming the melt rate is proportional to the thermal driving multiplied by the boundary layer velocity (Bradley et al., 2022; Millgate et al., 2013), it is informative to examine the modeled glacier-adjacent temperatures and (ice-tangential) horizontal velocities, not including velocities associated with the vertical plume (Fig. 11.) We find that temperatures are increased on average over summer and autumn (6 months) with a sill present (SILL-PLUME) (Fig. 11). Horizontal speeds are similar between PLUME and SILL-PLUME scenarios, though there is an indication of higher horizontal speeds towards the south of Neumayer Glacier face. With no sill present, WB-PLUME decreases the water temperature adjacent to the glacier, whereas with a sill present WB-PLUME very slightly increases the water temperature near-bed (Fig. 11). We can reasonably infer that melt rates are likely to be higher for SILL-PLUME than PLUME due to the warmer waters (increased thermal driving) adjacent to the glacier submarine face. In fact, the offline plume model predicts melt rates ~1 m/day greater in late summer/early autumn with the SILL-PLUME scenario within the vicinity of the theoretical plume, compared to the PLUME scenario (not shown). Therefore, the observed rapid retreat of Neumayer Glacier may be the consequence of a positive feedback, whereby warmer water is trapped and recirculated in the inner basin, promoting higher submarine melt rates through increased thermal driving. Increased submarine melting will both increase turbulence and reduce the density of the inner basin, driving a stronger inflow of warmer waters, thus promoting further melting through both increased ice-face boundary layer velocities and thermal driving. Additionally, warmer waters at depth may promote undercutting, which could lead to greater mass loss through calving (Benn et al., 2017). Interpretation of the results requires caution as the plume would also introduce high vertical velocities not captured in the ocean model, as well as increase the horizontal velocities regardless of the presence of a sill. The processes described here, and the proposed positive feedback mechanism, are not

present in EB as the inner sill peak is much deeper. This might explain why Nordenskjöld Glacier has remained relatively stable in the presence of oceanic variability that is apparently uniform across the two fjord arms.

The hypothesis of a positive feedback mechanism involving an inner sill is supported by observations of the front positions of Neumayer Glacier. The terminus stayed relatively stable in the vicinity of the postulated sill between 1955 and 1989, followed by rapid retreat once the

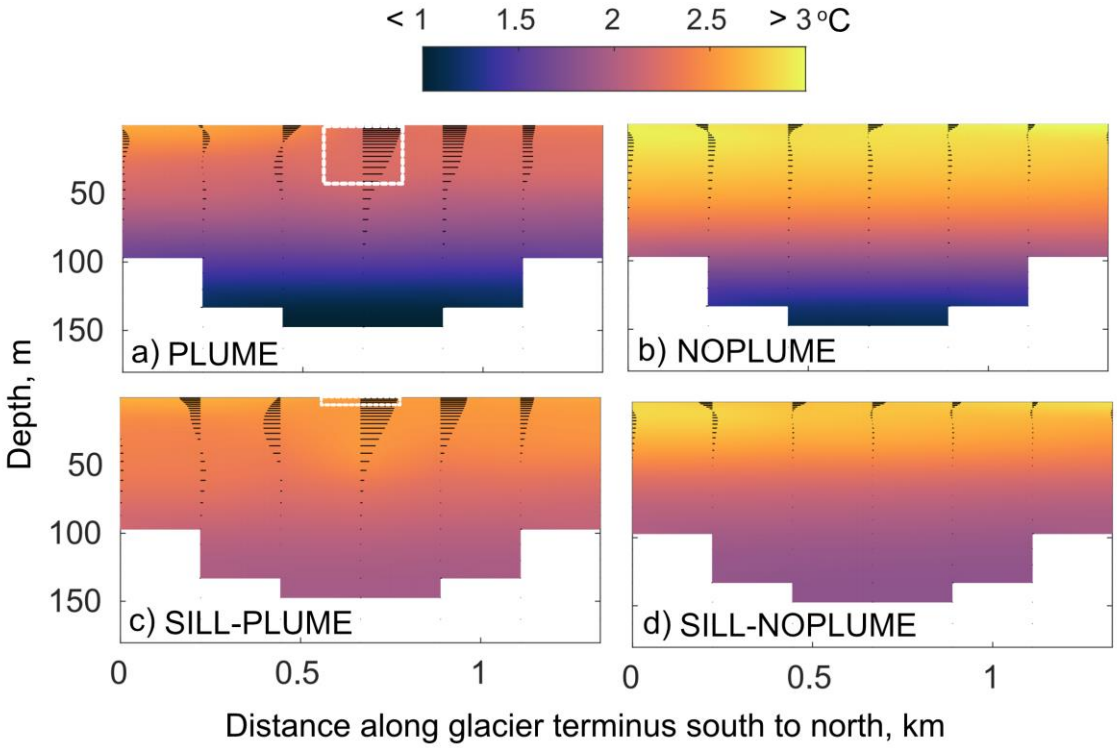

Figure 11. 6-month average (December 2005 to May 2006) of conservative temperature (shading) and horizontal velocities (black lines) adjacent to Neumayer Glacier, drawn facing the glacier terminus for (a) PLUME, (b) NOPLUME, (c) SILL-PLUME and (d) SILL-NOPLUME. The largest area over which WB-PLUME is inserted during this time period is highlighted by the white dashed boxes in (a) and (c).

glacier had moved behind the sill (Cook et al., 2010). However, it remains unclear what caused Neumayer Glacier to retreat past the sill in the first instance. Further exploration of this hypothesis requires a more comprehensive study, including detailed bathymetric surveys of the head of WB up to Neumayer Glacier terminus and a more accurate model representation of the WB inner sill. Future modeling work could be greatly enhanced by the development of an ice-ocean-atmosphere coupled model at higher spatial resolution.

In previous studies focused on Greenland fjords, the presence of a shallow sill has been shown to reduce the melting of tidewater glaciers due to colder waters overlaying warmer waters (Millan et al., 2018; Schaffer et al., 2020). We find that in fjord systems where warmer waters overlay colder waters the opposite holds and a shallow sill may promote higher melt rates.

5 Conclusions

This study combines observational data and a new high-resolution validated model of Cumberland Bay, South Georgia, to greatly improve the understanding of the oceanographic variability and the drivers of glacier retreat. Results show that the seasonal cycle is strongly influenced by freshwater forcing via subglacial plumes. The difference in bathymetry between Cumberland Bay's two fjord arms, West Bay and East Bay, results in differing signals of buoyancy-driven outflow. The possible presence of an inner sill in West Bay alters the seasonal variability in buoyancy-driven outflow and the properties within the inner basin. We find evidence to suggest that the rapid retreat of Neumayer Glacier in West Bay, compared to Nordenskjöld Glacier in East Bay, might be explained by the trapping of warmer waters adjacent to the glacier by a postulated inner sill, with a possible positive feedback mechanism enhancing glacial melt. Further study is required to test this hypothesis, through the acquisition of accurate bathymetric data over the sill in West Bay together with a coupled ice-ocean-atmosphere model at higher resolution. With the use of the new model as a tool, future studies can identify other key drivers of variability in circulation and shelf exchange, as well as investigate interannual variability that may have triggered the retreat.

The fjord circulation patterns identified in this study have wider implications beyond glacier retreat. For example, the seasonality of buoyancy-driven outflow and the cross-fjord flow

variability suggest the transport and retention of fish larvae will be sensitive to the timing and location of egg hatching. The availability of iron for downstream phytoplankton blooms derived from glacial flour plumes may be limited by a subsurface terminating plume or the presence of a sill acting as a barrier. This study is a fundamental step toward understanding the implications of oceanographic variability for glacier dynamics in Cumberland Bay, whilst providing a tool for investigating the impact of oceanographic variability on the marine ecosystem at South Georgia.

Acknowledgments

This work was supported by the Natural Environment Research Council via the BAS Polar Oceans program and the INSPIRE Doctoral Training Partnership. The authors would like to thank Polar Seafish Ltd for additional support and funding. We thank the Government of South Georgia and the South Sandwich Islands and the crew of the Pharos SG for facilitating and aiding CTD data collection. The numerical simulations were carried out on the ARCHER2 UK National Supercomputing Service (https://www.archer2.ac.uk/).

Data availability statement

The data are currently available in the provided figures and tables. The observational data and model output underlying the figures and tables in this paper are in the process of being made available through the UK Polar Data Centre. The model code for NEMO-4.0.6 is available from the NEMO website (**www.nemo-ocean.eu**).

631

632 **References**

633 Bartholomaus, T. C., Stearns, L. A., Sutherland, D. A., Shroyer, E. L., Nash, J. D., Walker, R. T.,
634 Catania, G., Felikson, D., Carroll, D., Fried, M. J., Noël, B. P. Y., & van den Broeke, M. R.
635 (2016). Contrasts in the response of adjacent fjords and glaciers to ice-sheet surface melt in
636 West Greenland. *Annals of Glaciology*, *57*(73), 25–38. https://doi.org/10.1017/aog.2016.19

637 Benn, D. I., Cowton, T., Todd, J., & Luckman, A. (2017). Glacier Calving in Greenland. In
638 *Current Climate Change Reports* (Vol. 3, Issue 4). https://doi.org/10.1007/s40641-017-
639 0070-1

640 Berntsen, J., Xing, J., & Davies, A. M. (2009). *Numerical studies of flow over a sill : sensitivity*
641 *of the non-hydrostatic effects to the grid size*. 1043–1059. https://doi.org/10.1007/s10236-
642 009-0227-0

643 Boone, W., Rysgaard, S., Kirillov, S., Dmitrenko, I., Bendtsen, J., Mortensen, J., Meire, L.,
644 Petrusevich, V., & Barber, D. G. (2017). Circulation and fjord-shelf exchange during the
645 ice-covered period in Young Sound-Tyrolerfjord, Northeast Greenland (74°N). *Estuarine,*
646 *Coastal and Shelf Science*, *194*, 205–216. https://doi.org/10.1016/j.ecss.2017.06.021

647 Bradley, A. T., Bett, D. T., Dutrieux, P., de Rydt, J., & Holland, P. R. (2022). The Influence of
648 Pine Island Ice Shelf Calving on Basal Melting. *Journal of Geophysical Research: Oceans*,
649 *127*(9). https://doi.org/10.1029/2022JC018621

650 Carroll, D., Sutherland, D. A., Shroyer, E. L., Nash, J. D., Catania, G. A., & Stearns, L. A.
651 (2015). Modeling turbulent subglacial meltwater plumes: Implications for fjord-scale
652 buoyancy-driven circulation. *Journal of Physical Oceanography*.
653 https://doi.org/10.1175/JPO-D-15-0033.1

654 Catania, G. A., Stearns, L. A., Sutherland, D. A., Fried, M. J., Bartholomaus, T. C., Morlighem,
655 M., Shroyer, E., & Nash, J. (2018). Geometric Controls on Tidewater Glacier Retreat in
656 Central Western Greenland. *Journal of Geophysical Research: Earth Surface*, *123*(8),
657 2024–2038. https://doi.org/10.1029/2017JF004499

Christoffersen, P., Mugford, R. I., Heywood, K. J., Joughin, I., Dowdeswell, J. A., Syvitski, J. P. M., Luckman, A., & Benham, T. J. (2011). Warming of waters in an East Greenland fjord prior to glacier retreat: Mechanisms and connection to large-scale atmospheric conditions. *Cryosphere*. https://doi.org/10.5194/tc-5-701-2011

Chu, V. W. (2014). Greenland ice sheet hydrology: A review. *Progress in Physical Geography*, *38*(1). https://doi.org/10.1177/0309133313507075

Cook, A. J., Poncet, S., Cooper, A. P. R., Herbert, D. J., & Christie, D. (2010). Glacier retreat on South Georgia and implications for the spread of rats. *Antarctic Science*, *22*(3), 255–263. https://doi.org/10.1017/S0954102010000064

Cottier, F. R., Nilsen, F., Skogseth, R., Tverberg, V., Skardhamar, J., & Svendsen, H. (2010). Arctic fjords: A review of the oceanographic environment and dominant physical processes. *Geological Society Special Publication*, *344*(November), 35–50. https://doi.org/10.1144/SP344.4

Cowton, T., Slater, D., Sole, A., Goldberg, D., & Nienow, P. (2015). Modeling the impact of glacial runoff on fjord circulation and submarine melt rate using a new subgrid-scale parameterization for glacial plumes. *Journal of Geophysical Research: Oceans*. https://doi.org/10.1002/2014JC010324

DAVIES, H. (1976). A lateral boundary formulation for multi-level prediction models. *Quarterly Journal of the Royal Meteorological Society*, *102*(432). https://doi.org/10.1256/smsqj.43209

Davison, B. J., Cowton, T. R., Cottier, F. R., & Sole, A. J. (2020). Iceberg melting substantially modifies oceanic heat flux towards a major Greenlandic tidewater glacier. *Nature Communications*, *11*(1). https://doi.org/10.1038/s41467-020-19805-7

Egbert, G. D., & Erofeeva, S. Y. (2002). Efficient inverse modeling of barotropic ocean tides. *Journal of Atmospheric and Oceanic Technology*. https://doi.org/10.1175/1520-0426(2002)019<0183:EIMOBO>2.0.CO;2

ENGEDAHL, H. (1995). Use of the flow relaxation scheme in a three-dimensional baroclinic ocean model with realistic topography. *Tellus A*, *47*(3). https://doi.org/10.1034/j.1600-0870.1995.t01-2-00006.x

686 Everson, I. (1992). Managing Southern Ocean krill and fish stocks in a changing
687 environment. *Philosophical Transactions - Royal Society of London, B*, *338*(1285), 311–
688 317. https://doi.org/10.1098/rstb.1992.0151

689 Everson, I., North, A. W., Paul, A., Cooper, R., McWilliam, N. C., & Kock, K. H. (2001).
690 Spawning locations of mackerel icefish at South Georgia. *CCAMLR Science*.

691 Flather, R. A. (1994). A storm surge prediction model for the northern Bay of Bengal with
692 application to the cyclone disaster in April 1991. *Journal of Physical Oceanography*, *24*(1).
693 https://doi.org/10.1175/1520-0485(1994)024<0172:ASSPMF>2.0.CO;2

694 Fraser, N. J., & Inall, M. E. (2018). Influence of Barrier Wind Forcing on Heat Delivery Toward
695 the Greenland Ice Sheet. *Journal of Geophysical Research: Oceans*, *123*(4), 2513–2538.
696 https://doi.org/10.1002/2017JC013464

697 Gade, H. G. (1979). Melting of Ice in Sea Water: A Primitive Model with Application to the
698 Antarctic Ice Shelf and Icebergs. *Journal of Physical Oceanography*, *9*(1).
699 https://doi.org/10.1175/1520-0485(1979)009<0189:moiisw>2.0.co;2

700 Gordon, J. E., Haynes, V. M., & Hubbard, A. (2008). Recent glacier changes and climate trends
701 on South Georgia. *Global and Planetary Change*, *60*(1–2), 72–84.
702 https://doi.org/10.1016/j.gloplacha.2006.07.037

703 Hager, A. O., Sutherland, D. A., Amundson, J. M., Jackson, R. H., Kienholz, C., Motyka, R. J.,
704 & Nash, J. D. (2022). Subglacial Discharge Reflux and Buoyancy Forcing Drive
705 Seasonality in a Silled Glacial Fjord. *Journal of Geophysical Research: Oceans*, *127*(5).
706 https://doi.org/10.1029/2021JC018355

707 Hersbach, H., Bell, B., Berrisford, P., Hirahara, S., Horányi, A., Muñoz-Sabater, J., Nicolas, J.,
708 Peubey, C., Radu, R., Schepers, D., Simmons, A., Soci, C., Abdalla, S., Abellan, X.,
709 Balsamo, G., Bechtold, P., Biavati, G., Bidlot, J., Bonavita, M., … Thépaut, J. N. (2020).
710 The ERA5 global reanalysis. *Quarterly Journal of the Royal Meteorological Society*,
711 *146*(730). https://doi.org/10.1002/qj.3803

712 Hewitt, I. J. (2020). Subglacial Plumes. *Annual Review of Fluid Mechanics*, *52*(1), 145–169.
713 https://doi.org/10.1146/annurev-fluid-010719-060252

Hodgson, D. A., Graham, A. G. C., Grif, H. J., Roberts, S. J., Cofaigh, C. Ó., Bentley, M. J., & Evans, D. J. A. (2014). *Glacial history of sub-Antarctic South Georgia based on the submarine geomorphology of its fjords q*. *89*, 129–147. https://doi.org/10.1016/j.quascirev.2013.12.005

Hogg, O. T., Huvenne, V. A. I., Griffiths, H. J., Dorschel, B., & Linse, K. (2016). Landscape mapping at sub-Antarctic South Georgia provides a protocol for underpinning large-scale marine protected areas. *Scientific Reports*, *6*. https://doi.org/10.1038/srep33163

Holland, D. M., & Jenkins, A. (1999). Modeling thermodynamic ice-ocean interactions at the base of an ice shelf. *Journal of Physical Oceanography*, *29*(8 PART 1). https://doi.org/10.1175/1520-0485(1999)029<1787:mtioia>2.0.co;2

Hollingsworth, A., Kållberg, P., Renner, V., & Burridge, D. M. (1983). An internal symmetric computational instability. *Quarterly Journal of the Royal Meteorological Society*, *109*(460). https://doi.org/10.1002/qj.49710946012

Holmes, T. M., Wuttig, K., Chase, Z., Schallenberg, C., van der Merwe, P., Townsend, A. T., & Bowie, A. R. (2019). Glacial and hydrothermal sources of dissolved iron(II) in Southern Ocean waters surrounding Heard and McDonald Islands. In *In Prep.* (Issue Ii). https://doi.org/10.1029/2020JC016286

Holt, J. T., Allen, J. I., Proctor, R., & Gilbert, F. (2005). Error quantification of a high-resolution coupled hydrodynamic-ecosystem coastal-ocean model: Part 1 model overview and assessment of the hydrodynamics. *Journal of Marine Systems*, *57*(1–2). https://doi.org/10.1016/j.jmarsys.2005.04.008

Jenkins, A. (2011). Convection-driven melting near the grounding lines of ice shelves and tidewater glaciers. *Journal of Physical Oceanography*. https://doi.org/10.1175/JPO-D-11-03.1

Large, W. G., & Yeager, S. G. (2004). Diurnal to decadal global forcing for ocean and sea-ice models: the data sets and flux climatologies. *Ech. Rep., NCAR Climate and Global Dynamics Division; Boulder, CO, United States*.

741 Lin, P., Pickart, R. S., Torres, D. J., & Pacini, A. (2018). Evolution of the freshwater coastal
742 current at the Southern Tip of Greenland. *Journal of Physical Oceanography*, *48*(9).
743 https://doi.org/10.1175/JPO-D-18-0035.1

744 Luckman, A., Benn, D. I., Cottier, F., Bevan, S., Nilsen, F., & Inall, M. (2015). Calving rates at
745 tidewater glaciers vary strongly with ocean temperature. *Nature Communications*, *6*.
746 https://doi.org/10.1038/ncomms9566

747 Meredith, M. P., Brandon, M. A., Murphy, E. J., Trathan, P. N., Thorpe, S. E., Bone, D. G.,
748 Chernyshkov, P. P., & Sushin, V. A. (2005). Variability in hydrographic conditions to the
749 east and northwest of South Georgia, 1996-2001. *Journal of Marine Systems*.
750 https://doi.org/10.1016/j.jmarsys.2004.05.005

751 Millan, R., Rignot, E., Mouginot, J., Wood, M., Bjørk, A. A., & Morlighem, M. (2018).
752 Vulnerability of Southeast Greenland Glaciers to Warm Atlantic Water From Operation
753 IceBridge and Ocean Melting Greenland Data. *Geophysical Research Letters*, *45*(6).
754 https://doi.org/10.1002/2017GL076561

755 Millgate, T., Holland, P. R., Jenkins, A., & Johnson, H. L. (2013). The effect of basal channels
756 on oceanic ice-shelf melting. *Journal of Geophysical Research: Oceans*, *118*(12).
757 https://doi.org/10.1002/2013JC009402

758 Mortensen, J., Bendtsen, J., Motyka, R. J., Lennert, K., Truffer, M., Fahnestock, M., &
759 Rysgaard, S. (2013). On the seasonal freshwater stratification in the proximity of fast-
760 flowing tidewater outlet glaciers in a sub-Arctic sill fjord. *Journal of Geophysical*
761 *Research: Oceans*, *118*(3). https://doi.org/10.1002/jgrc.20134

762 Mortensen, J., Lennert, K., Bendtsen, J., & Rysgaard, S. (2011). Heat sources for glacial melt in
763 a sub-Arctic fjord (Godthåbsfjord) in contact with the Greenland Ice Sheet. *Journal of*
764 *Geophysical Research: Oceans*, *116*(1), 1–13. https://doi.org/10.1029/2010JC006528

765 Motyka, R. J., Cassotto, R., Truffer, M., Kjeldsen, K. K., van As, D., Korsgaard, N. J.,
766 Fahnestock, M., Howat, I., Langen, P. L., Mortensen, J., Lennert, K., & Rysgaard, S. (2017).
767 Asynchronous behavior of outlet glaciers feeding Godthåbsfjord (Nuup Kangerlua) and the
768 triggering of Narsap Sermia's retreat in SW Greenland. *Journal of Glaciology*, *63*(238).
769 https://doi.org/10.1017/jog.2016.138

Okubo, A. (1971). Oceanic diffusion diagrams. *Deep Sea Research and Oceanographic Abstracts*, *18*(8), 789–802. https://doi.org/10.1016/0011-7471(71)90046-5

O'Leary, M., & Christoffersen, P. (2013). Calving on tidewater glaciers amplified by submarine frontal melting. *Cryosphere*. https://doi.org/10.5194/tc-7-119-2013

Orsi, A. H., Whitworth, T., & Nowlin, W. D. (1995). On the meridional extent and fronts of the Antarctic Circumpolar Current. *Deep-Sea Research Part I*, *42*(5). https://doi.org/10.1016/0967-0637(95)00021-W

Penduff, T., le Sommer, J., Barnier, B., Treguier, A. M., Molines, J. M., & Madec, G. (2007). Influence of numerical schemes on current-topography interactions in 1/4° global ocean simulations. *Ocean Science*, *3*(4). https://doi.org/10.5194/os-3-509-2007

Schaffer, J., Kanzow, T., von Appen, W. J., von Albedyll, L., Arndt, J. E., & Roberts, D. H. (2020). Bathymetry constrains ocean heat supply to Greenland's largest glacier tongue. *Nature Geoscience*, *13*(3). https://doi.org/10.1038/s41561-019-0529-x

Sciascia, R., Straneo, F., Cenedese, C., & Heimbach, P. (2013). *Seasonal variability of submarine melt rate and circulation in an East Greenland fjord*. *118*(May), 2492–2506. https://doi.org/10.1002/jgrc.20142

Silvano, A., Rintoul, S. R., Peña-Molino, B., & Williams, G. D. (2017). Distribution of water masses and meltwater on the continental shelf near the Totten and Moscow University ice shelves. *Journal of Geophysical Research: Oceans*, *122*(3). https://doi.org/10.1002/2016JC012115

Slater, D. A., Nienow, P. W., Cowton, T. R., Goldberg, D. N., & Sole, A. J. (2015). Effect of near-terminus subglacial hydrology on tidewater glacier submarine melt rates. *Geophysical Research Letters*, *42*(8). https://doi.org/10.1002/2014GL062494

Slater, D. A., Nienow, P. W., Goldberg, D. N., Cowton, T. R., & Sole, A. J. (2017). A model for tidewater glacier undercutting by submarine melting. *Geophysical Research Letters*. https://doi.org/10.1002/2016GL072374

Sommer, U., & Lengfellner, K. (2008). Climate change and the timing, magnitude, and composition of the phytoplankton spring bloom. *Global Change Biology*. https://doi.org/10.1111/j.1365-2486.2008.01571.x

799 Soontiens, N., & Allen, S. E. (2017). Modelling sensitivities to mixing and advection in a sill-
800 basin estuarine system. *Ocean Modelling*, *112*, 17–32.
801 https://doi.org/10.1016/j.ocemod.2017.02.008

802 Soontiens, N., Allen, S. E., Latornell, D., le Souëf, K., MacHuca, I., Paquin, J. P., Lu, Y.,
803 Thompson, K., & Korabel, V. (2016). Storm Surges in the Strait of Georgia Simulated with
804 a Regional Model. *Atmosphere - Ocean*, *54*(1), 1–21.
805 https://doi.org/10.1080/07055900.2015.1108899

806 Staalstrøm, A., & Petter, L. (2016). Vertical mixing and internal wave energy fluxes in a sill
807 fjord. *Journal of Marine Systems*, *159*, 15–32.
808 https://doi.org/10.1016/j.jmarsys.2016.02.005

809 Straneo, F., & Cenedese, C. (2015). The dynamics of greenland's glacial fjords and their role in
810 climate. *Annual Review of Marine Science*, *7*. https://doi.org/10.1146/annurev-marine-
811 010213-135133

812 Straneo, F., Hamilton, G. S., Sutherland, D. A., Stearns, L. A., Davidson, F., Hammill, M. O.,
813 Stenson, G. B., & Rosing-asvid, A. (2010). Rapid circulation of warm subtropical waters in
814 a major glacial fjord in East Greenland. *Nature Geoscience*, *3*(February).
815 https://doi.org/10.1038/ngeo764

816 Umlauf, L., & Burchard, H. (2003). A generic length-scale equation for geophysical turbulence
817 models. *Journal of Marine Research*, *61*(2). https://doi.org/10.1357/002224003322005087

818 Venables, H. J., Meredith, M. P., & Brearley, J. A. (2017). Modification of deep waters in
819 Marguerite Bay, western Antarctic Peninsula, caused by topographic overflows. *Deep-Sea*
820 *Research Part II: Topical Studies in Oceanography*, *139*.
821 https://doi.org/10.1016/j.dsr2.2016.09.005

822 Ward, P. (1989). The distribution of zooplankton in an Antarctic fjord at South Georgia during
823 summer and winter. *Antarctic Science*, *1*(2). https://doi.org/10.1017/S0954102089000210

824 Wesławski, J. M., Kendall, M. A., Włodarska-Kowalczuk, M., Iken, K., Kedra, M., Legezynska,
825 J., & Sejr, M. K. (2011). Climate change effects on Arctic fjord and coastal macrobenthic
826 diversity-observations and predictions. In *Marine Biodiversity* (Vol. 41, Issue 1).
827 https://doi.org/10.1007/s12526-010-0073-9

Węsławski, J. M., Pedersen, G., Petersen, S. F., & Poraziński, K. (2000). Entrapment of macroplankton in an Arctic fjord basin, Kongsfjorden, Svalbard. *Oceanologia*, *42*(1), 57–69.

Winder, M., & Sommer, U. (2012). Phytoplankton response to a changing climate. In *Hydrobiologia*. https://doi.org/10.1007/s10750-012-1149-2

Young, E. F., Meredith, M. P., Murphy, E. J., & Carvalho, G. R. (2011). High-resolution modelling of the shelf and open ocean adjacent to South Georgia, Southern Ocean. *Deep-Sea Research Part II: Topical Studies in Oceanography*, *58*(13–16). https://doi.org/10.1016/j.dsr2.2009.11.003

Young, E. F., Thorpe, S. E., Banglawala, N., & Murphy, E. J. (2014). Variability in transport pathways on and around the South Georgia shelf, Southern Ocean: Implications for recruitment and retention. *Journal of Geophysical Research: Oceans*, *119*(1), 241–252. https://doi.org/10.1002/2013JC009348

Young, E., Murphy, E., & Trathan, P. (2016). High-resolution ocean modelling of the South Georgia and South Orkney Islands regions. *WG-EMM-16/15. CCAMLR Working Group on Ecosystem Monitoring and Management. Report of the XXXV Scientific Committee, Bologna, Italy.*

Oceanographic variability in Cumberland Bay, South Georgia, and its implications for glacier retreat

Joanna C. Zanker[1], Emma. Young[1], Paul. R. Holland[1], Ivan D. Haigh[2], Paul Brickle[3]

[1]British Antarctic Survey, Cambridge, UK. [2]Ocean and Earth Science, National Oceanography Centre, University of Southampton, Southampton, UK. [3]South Atlantic Environmental Research Institute, Stanley, FI.

Corresponding author: Joanna C. Zanker (joazan@bas.ac.uk)

Key Points:

- Observational data and a new high-resolution model are combined to describe oceanographic variability in Cumberland Bay, South Georgia.
- We show that buoyancy-driven subglacial outflow plumes are a key driver of seasonal variability and spatial differences between fjord arms.
- We highlight that the presence of a postulated inner sill may be a key factor in the observed rapid glacier retreat.

Abstract

South Georgia is a heavily glaciated sub-Antarctic island in the Southern Ocean. Cumberland Bay is the largest fjord on the island, split into two arms, each with a large marine-terminating glacier at the head. Although these glaciers have shown markedly different retreat rates over the past century, the underlying drivers of such differential retreat are not yet understood. This study uses observations and a new high-resolution oceanographic model to characterize oceanographic variability in Cumberland Bay and to explore its influence on glacier retreat. While observations indicate a strong seasonal cycle in temperature and salinity, they reveal no clear hydrographic differences that could explain the differential glacier retreat. Model simulations suggest the subglacial outflow plume dynamics and fjord circulation are sensitive to the bathymetry adjacent to the glacier. The addition of a postulated shallow inner sill in one fjord arm significantly changes the water properties in the resultant inner basin by blocking the intrusion of colder, higher salinity waters at depth. This increase in temperature could accelerate both the subglacial plume-driven melt, and the melting of the wider submarine ice face, which is proposed as a possible explanation for the different rates of glacier retreat observed in the two fjord arms. This study represents the first detailed description of the oceanographic variability of a sub-Antarctic island fjord, highlighting the sensitivity of plume dynamics to bathymetry. Notably, in fjords systems where temperature decreases with depth, the presence of a shallow sill has the potential to accelerate glacier retreat.

Plain Language Summary

Cumberland Bay, a fjord on the sub-Antarctic island of South Georgia, is split into two arms, each with a large marine-terminating glacier. One of these glaciers is retreating much faster than the other, possibly due to differences in oceanography between the arms. Here, we investigate how the oceanography in Cumberland Bay varies seasonally and with the seabed depth by using oceanographic data and numerical ocean simulations. We find that the properties of buoyant plumes, which arise from meltwater entering the ocean from beneath the glacier, are sensitive to the seabed depth near the glaciers, resulting in strong differences in ocean flow between the fjord arms. Assuming higher ocean temperatures increase glacier melting, we find that the presence of a near-glacier shallow sill likely increases melting by blocking deeper, colder waters and trapping warmer surface waters close to the glacier. As a shallow sill is likely to be present near

the rapidly retreating glacier only, this result offers a persuasive explanation for the observed glacier retreat. Understanding the variability in oceanography and glacier retreat is important as they directly impact the marine ecosystem at South Georgia by influencing the availability of nutrients for primary production and food availability for higher predators.

1 Introduction

Fjords are a common feature of high-latitude coastlines and have high biological productivity. In the Arctic, fjords are found in Alaska, Svalbard, and Greenland, for example. In the Southern Hemisphere, fjords are found in Patagonia, New Zealand, Antarctica, and on sub-Antarctic islands. High-latitude fjords are usually associated with seasonal sea ice and, in most cases, have a glacier terminating at the fjord head (Cottier et al., 2010). Fjord circulation directly governs the stability of tidewater (grounded) glaciers (Cottier et al., 2010), frontal ablation of which directly contributes to sea-level rise (Benn et al., 2017).

Marine ecosystems in fjords support large colonies of higher predators such as sea birds and marine mammals (Ward, 1989; Węsławski et al., 2000), while open ocean and on-shelf phytoplankton blooms may also rely on the transport of nutrients circulated by nearby fjords from upwelling and terrestrial sources via glacial runoff (Holmes et al., 2019; Węsławski et al., 2000). Fjords are also important spawning grounds for fish (Everson et al., 2001). Recruitment and retention of fish larvae are controlled by fjord circulation and shelf exchange, an understanding of which is vital for the management of local fisheries (Everson, 1992). In our changing climate, frontal ablation of tidewater glaciers is expected to increase (Christoffersen et al., 2011; Mortensen et al., 2011; Straneo et al., 2010), the composition and extent of phytoplankton blooms are expected to change substantially (Sommer & Lengfellner, 2008; Winder & Sommer, 2012) and the changes in fjord circulation are likely to impact a diversity of ecosystem responses, such as fish larvae retention (Wesławski et al., 2011). Therefore, understanding fjord systems is crucial.

In this paper, we focus on South Georgia, a sub-Antarctic island in the Southern Ocean which is heavily glaciated and indented with fjords. The island lies in the path of the Antarctic Circumpolar Current (ACC), which flows unimpeded around the Southern Ocean, driven by strong westerly winds (Orsi et al., 1995). The Polar Front lies to the north of the island and the

Southern Antarctic Circumpolar Current Front (SACCF) loops anticyclonically around the island from the south before retroflecting to the east (Fig. 1a) (Meredith et al., 2005). While the island lies beyond the winter sea-ice limit, it does see the formation of intermittent seasonal pancake ice. Cumberland Bay, situated on the northeast coast, is the largest fjord on the island and is characterized by two arms, East Bay and West Bay (Fig 1a, green square). Cumberland East Bay (EB) is approximately 15 km long and 3-5 km wide with a maximum depth of 270 m. Nordenskjöld Glacier terminates at the head of EB and there is a shallow inner basin with a prominent inner basin sill (Hodgson et al., 2014, Fig. 4). An outer basin sill, which is partially eroded near the center, marks the edge of the outer basin (Fig. 1c). Cumberland West Bay (WB) is approximately 18 km long and 2.5 - 5 km wide, with a maximum depth of 265 m. Neumayer Glacier terminates at the head of West Bay. The outer basin sill of WB is heavily eroded towards the southern half of the fjord (Hodgson et al., 2014). Bathymetric surveys have not extended close enough to the glacier to identify an inner basin sill (Hodgson et al., 2014), though chart data (Admiralty Chart 3588, Approaches to Stromness and Cumberland Bay) include shallow points (~30 m) extending the width of WB in the area highlighted in Fig. 1c (white dashed lines). We believe these data indicate a sill, and for the remainder of this paper, this is referred to as the 'postulated' inner sill.

Neumayer and Nordenskjöld Glaciers have shown markedly different rates of retreat over the past century (Cook et al., 2010; Gordon et al., 2008), with Neumayer Glacier retreating more than 10 km since 1955 and Nordenskjöld Glacier only ~2 km in the same time period. Cook et al. (2008) showed that the front position of Neumayer Glacier was relatively stable between 1955 and 1990, with the front in the vicinity of the postulated inner sill, but the mean rate of change in the front position increased rapidly between 1990 and 2008. It is not yet understood why these glaciers are showing such different rates of mass loss. However, plume dynamics and submarine melting may be key contributing factors, as studies of other high-latitude fjord systems have shown (Cowton et al., 2015; Motyka et al., 2017).

Previous work has demonstrated that an increase in submarine melting is a key driver of the observed increase in mass loss of tidewater glaciers in recent years, both directly through increased melt and indirectly by altering the ice front shape such that the rate of calving is increased (e.g., Luckman et al., 2015; O'Leary & Christoffersen, 2013). The melt rate is

approximately proportional to the difference between the temperature of the water and the ice freezing temperature (thermal driving) and the speed of the flow at the ice-ocean interface (boundary layer velocity) (Holland & Jenkins, 1999; Millgate et al., 2013). These quantities depend on the wider circulation regime within the fjord. Factors influencing the circulation regime include fjord-shelf exchange, atmospheric forcing, surface freshwater runoff, subglacial discharge, and fjord geometry, such as bathymetric sills (e.g., Bartholomaus et al., 2016; Boone et al., 2017; Catania et al., 2018; Cottier et al., 2010; Fraser & Inall, 2018; Hager et al., 2022; Mortensen et al., 2011). Fjord circulation patterns are complex and there is a lack of clear understanding of how the interactions between these processes lead to glacier retreat, particularly in fjord systems where warm water overlays colder water, such as in Cumberland Bay. This temperature structure is unusual for high-latitude fjords, which are generally characterized by cold, fresh waters from ice sheet runoff overlaying warmer waters (Lin et al., 2018; Silvano et al., 2017).

Oceanic melting of tidewater glaciers is enhanced when subglacial discharge meets the ocean and rises as a buoyant plume in contact with the submarine ice face (Slater et al., 2015). Subglacial discharge arises from surface glacial meltwater that has been directed through moulins and crevasses on the ice surface to reach the bed and then fed through a system of subglacial channels towards the glacier's grounding line, along with direct basal glacier melt (Chu, 2014). The discharge enters the ocean and entrains ambient ocean water generating inflow at depth as it rises as a buoyant plume in contact with the ice (Jenkins, 2011). The plume reaches either neutral density or the ocean surface, resulting in a thick flow away from the glacier. The inflow and outflow generated by the subglacial discharge is known as buoyancy-driven circulation (Carroll et al., 2015; Straneo & Cenedese, 2015). The interaction between buoyancy-driven circulation and submarine sills has the potential to alter the water circulation and the heat available for melting at the submarine face, as the sill acts as a barrier to ocean currents (Hager et al., 2022; Holland & Jenkins, 1999). This interaction may give rise to spatial differences in fjord systems with multiple glaciers and complex bathymetry and is likely to change with the seasonally varying rate of subglacial discharge (Bartholomaus et al., 2016).

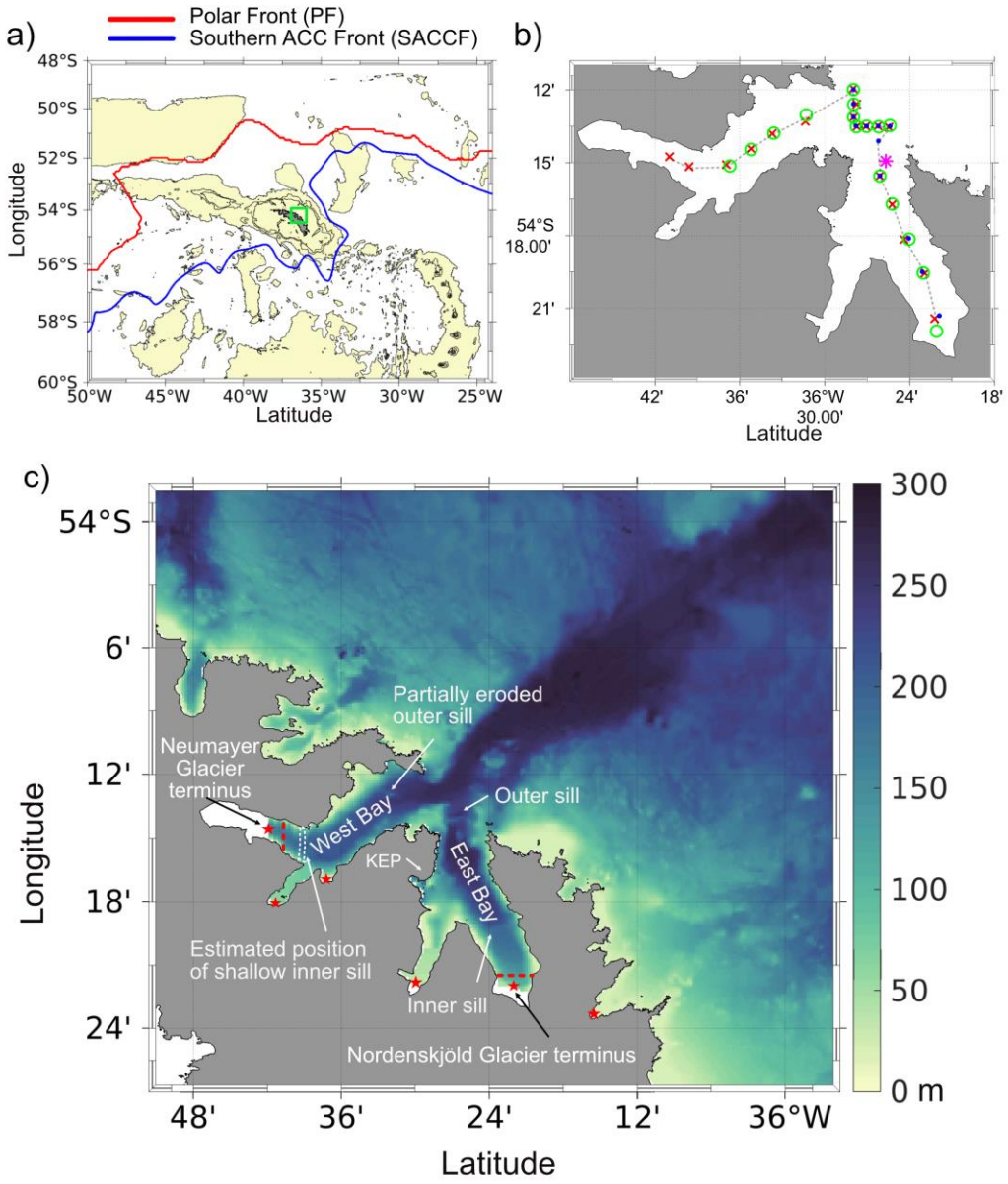

Figure 1. (a) Location of South Georgia in the Southern Ocean, with contours at 300, 1000, and 3000 m, and depths shallower than 3000 m shaded. Climatological locations of the Polar Front and Southern ACC Front are illustrated (Thorpe, 2001) and the location of Cumberland Bay is shown with the green square. (b) Positions of oceanographic surveys in Cumberland Bay from April 2012 (blue dots), February 2020 (green circles), November 2021 (red crosses), and January to November 2006 (pink star), and transect used for plotting data (grey dash line). (c) Cumberland Bay model domain, with bathymetry shaded (Hogg et al. 2016). Important bathymetric features are labelled, locations of glacier meltwater input are marked (red stars) and the locations of the cross-sections used for volume transport calculations are shown (red dashed lines).

132

In this study, we use oceanographic observations from Cumberland Bay and a new high-resolution ocean model (section 2) to address two main objectives. The first objective is to describe the seasonal and spatial variability between the two fjord arms, providing the first detailed study of this fjord system (section 3.1). The second objective is to identify key drivers of oceanographic variability that may influence glacier retreat, focussing on buoyancy-driven outflow and the presence of the postulated submarine sill (section 3.2). We then assess the limitations of the observations and modeling approach and discuss the implications of the results for understanding the rate of glacier retreat (section 4).

2 Data and methods

2.1 Observations

Four datasets of Conductivity Temperature Depth (CTD) data for Cumberland Bay from 2000 - 2021 were collated. These data provide information on the temporal and spatial variability of temperature and salinity in Cumberland Bay, as well as a resource for model validation. Firstly, CTD data were collected with irregular temporal frequency from five points in Cumberland East Bay between 2001 and 2006 by staff at King Edward Point station, using a Sea-Bird E19 (Fig 1b, pink star). Data from 2006 in the mouth of East Bay are chosen for analysis here, as this year and location had the best temporal coverage. Secondly, opportunistic CTD data were collected in Cumberland Bay on the 18th of April 2012 (JR272A) with a Sea-Bird E32 carousel water sampler (Fig. 1b, blue dots). Thirdly, between the 24th and 25th of February 2020 (DY113), a CTD survey was conducted with a Sea-Bird 9+ (Fig. 1b, red crosses). Finally, between the 9th and 14th of November 2021 (MV Pharos SG 12-21B) data were collected with a Valeport fastCTD (Fig. 1b, green circles). Data were processed by removing outliers, averaging into 2 m bins, and converting from in-situ temperature and practical salinity to conservative temperature and absolute salinity, respectively.

2.2 Oceanographic model

2.2.1 Model set up

A high-resolution Cumberland Bay model was built using the Nucleus for European Modeling of the Ocean version 4.0.6 (NEMO4), which solves the three-dimensional hydrostatic equations of motion for an incompressible fluid under the Boussinesq approximation on a structured computational grid. The vertical coordinate is represented with 35 vertical levels arranged as partial-cell z-levels. The levels are gradually stretched to achieve higher resolution in the surface layer, with a grid spacing near the surface of ~1 m reducing to ~30 m at depth. The domain is chosen to ensure the open boundaries are sufficiently far from the main region of interest (Cumberland Bay) to limit their influence, whilst allowing a good representation of variability in the wider shelf oceanography (Fig. 1c). Thus, the model domain extends to the shelf edge to the north, such that the maximum model depth does not exceed 300 m, and the western and eastern boundaries are positioned to capture a portion of the adjacent coastline (Young et al., 2014). A horizontal grid spacing of 1/500º latitude by 1/300º longitude (~200 m) is chosen with a resulting domain comprised of 280 by 240 grid cells in the horizontal. The resultant model is fine enough to resolve flows within Cumberland Bay whilst sufficiently computationally efficient for multi-year simulations.

NEMO4 uses the hydrostatic approximation, which saves considerably on computational expense. Although there are non-hydrostatic processes within the fjord, particularly over the sills, the effects are only likely to be resolved properly with a non-hydrostatic model if the horizontal grid spacing is significantly less than 100 m (Berntsen et al., 2009). However, a finer grid combined with the additional computational requirements of the non-hydrostatic solution would make the model too computationally expensive for multi-year simulations (Staalstrøm & Petter, 2016). A method for representing the subglacial plume using an offline model is described in section 2.2.4, which provides an efficient alternative for the representation of this non-hydrostatic process.

The model includes a free surface formulation and computational mode-splitting, with barotropic and baroclinic time steps of 1 s and 30 s, respectively. A free-slip lateral momentum boundary condition is used and the friction law at both the bathymetry and the ocean/atmosphere interface is assumed to be quadratic (non-linear) (Soontiens et al., 2016). A constant drag coefficient for surface and bed of 2.5×10^{-3} is chosen (Soontiens & Allen, 2017).

190 The Monotonic Upstream-centred Scheme for Conservation Laws (MUSCL) scheme is
191 used for tracer advection. The lateral diffusion scheme for tracers uses a rotated Laplacian
192 operator acting along iso-neutral surfaces. The lateral diffusive velocity and length scales are set
193 to 0.0009 ms^{-1} and 222 m respectively (Okubo, 1971). The lateral diffusion scheme for
194 momentum uses the bilaplacian operator acting in the horizontal (geopotential) direction with
195 lateral viscous velocity and length scales of 0.3 m s^{-1} and 222 m respectively. An energy and
196 enstrophy conserving scheme and the Hollingsworth correction are applied (Hollingsworth et al.,
197 1983; Penduff et al., 2007). The hydrostatic pressure gradient formulation is a Pressure Jacobian
198 scheme and the Generic Length Scale (GLS) scheme is used for the vertical turbulent mixing
199 (Umlauf & Burchard, 2003).

200 **2.2.2 Model bathymetry**

201 The model bathymetry was derived from a bathymetric dataset compiled by Hogg et al.
202 (2016) by averaging the 100 m resolution data onto the ~200 m grid (Fig. 1c). The main
203 bathymetric features - including the deep channels, shallow banks, and the coastal topography -
204 are mostly well captured at this resolution, with the exception that some small-scale features
205 (such as sills) are smoother than observed.

206 Official bathymetric data for the seabed exposed following the recent retreat of
207 Neumayer Glacier are not yet available. Shallow points in chart data and observed grounded
208 icebergs suggest a shallow inner sill exists, also hypothesized by Hodgson et al. (2014) and
209 referred to here as the 'postulated sill'. However, the width and depth of this potential sill are
210 unknown. Therefore, in the basic simulations, the choice was made to continue the known
211 shallow gradient of the bed topography towards the glacier terminus along the center of the fjord,
212 leading to a maximum depth of ~160 m adjacent to Neumayer Glacier. The adjacent data gaps
213 were filled by creating a quadratic 'U' shape across the fjord, assuming shallow coastal points of
214 20 m depth. This allows for an unrestricted channel for the simulated water flow. To consider the
215 impact of the postulated sill on the fjord oceanography, an artificial sill geometry was added for
216 a process test simulation. This was achieved by modifying the bathymetry such that it shallowed
217 steeply to 30 m across the width of the fjord, resulting in a bathymetric barrier one grid cell wide.
218 East Bay has more thorough coverage of observational bathymetry data, including close to
219 Nordenskjöld Glacier terminus, with a maximum depth of ~70 m adjacent to the glacier. A few

individual grid cells were altered to allow a gentle shallowing towards coastal edges of the fjord directly adjacent to the glacier and to give a smoother horizontal glacier terminus shape to aid model stability.

2.2.3 Open and surface boundary forcing

The model is forced at the open boundaries with tides from a global tidal model (TPXO9.2; (Egbert & Erofeeva, 2002) using eight tidal constituents (Q1, O1, P1, K1, N2, M2, S2, K2) and with 3D flows, sea surface height, temperature, and salinity derived from a regional South Georgia model (Young et al., 2016). Forcing data from the regional model are bilinearly interpolated to the open boundary points. The barotropic open boundary forcing uses the Flather Radiation Scheme (Flather, 1994). The baroclinic flows are treated with the 'zerograd' (Neumann) scheme where the values at the boundary are duplicated with no gradient. Tracers at the boundary use the Flow Relaxation Scheme which applies a simple relaxation of the model fields specified at the open boundary over a zone of 9 grid cells (Davies, 1976; Engedahl, 1995).

Surface boundary forcing is derived from the ERA5 reanalysis dataset with 30 km horizontal grid resolution (Hersbach et al., 2020). A bulk formulation (NCAR, Large & Yeager, 2004) is used. Interpolation of the coarse atmospheric forcing to the fine grid spacing of the model is achieved using the ‘on-the-fly’ option in NEMO4 and supplying a weights file for bilinear interpolation.

2.2.4 Terrestrial freshwater forcing

The freshwater contributions of surface run-off and sub-glacial outflow in the domain are taken from a theoretical climatological annual cycle calculated from historical precipitation data, glacier basin size, and positive degree days (Young et al., 2011). The freshwater flux for each glacier is injected into the appropriate ocean cell adjacent to the glacier and distributed over a prescribed depth range; the locations of glaciers contributing meltwater to the model are shown in Fig. 1c (red stars). For the two large marine-terminating glaciers in Cumberland Bay, the choice of depth range required consideration of subglacial meltwater plume-driven dynamics. Based on knowledge from other high-latitude ice masses, it is assumed that a majority of surface meltwater from the glaciers descends through crevasses and moulins and enters subglacial channel systems at the bed (Chu, 2014). These channels meet the ocean at the grounding line of the marine-terminating glaciers at the fjord head, leading to the rise of subglacial discharge as a

buoyant plume (Hewitt, 2020). The theoretical meltwater cycle is thus split into 10% surface runoff and 90% subglacial discharge. Given the uneven bathymetry, for the purposes of this modeling study it was assumed that 'localized channels' are formed, which emerge at the deepest part of the glacier termini over a width of one grid cell (~200 m) (Slater et al., 2015). In practice, buoyant plumes tend to rise in contact with the submarine ice face, causing melt and continue to entrain ambient ocean water until they reach neutral buoyancy (or the surface) where they intrude horizontally into the ocean (Hewitt, 2020; Sciascia et al., 2013). As NEMO4 uses the hydrostatic assumption, it is not possible to resolve the plume dynamics within the model, and so a parameterization is required.

The default option for meltwater runoff in NEMO4 is to introduce fresh, cold meltwater into the surface layers of the model, extending down to a specified depth. However, this does not capture potentially important increased buoyancy-driven outflow as a result of subglacial discharge, and could alter the ocean stratification unrealistically (Cottier et al., 2010). A new improvement has been developed for this study that adapts the freshwater input by incorporating the subglacial plume characteristics according to an offline plume model. This offline model requires ocean conditions, which necessitates an iterative process, as follows.

First, the model is run for 10 years (following a year spin-up) with no terrestrial freshwater forcing. The deepest ocean grid cell column adjacent to the glacier is identified as the point to which the subglacial discharge would be directed via the hydraulic gradient. Next, an offline plume model is run that calculates the properties of the plume based on Slater et al. (2017; equations 4a – 4d) and the melt rate of the submarine ice face, based on Jenkins (2011; equations 7 – 9). The plume model uses the temperature and salinity from the previously identified model grid cell column and the theoretical daily subglacial discharge, Q_S (Fig. 2a). Assuming values for the plume model constants following Slater et al., (2017), the model is solved for the temperature (T), salinity (S), volume (Q_P) and depth (D) at which the plume reaches neutral buoyancy (termination depth) (Fig. 2 b-e). Finally, the meltwater properties are set to the plume T and S and inserted into the relevant NEMO grid cell from the surface down to 10 m, or down to the termination depth D if the plume terminates below the surface. It is not currently possible to simulate a wholly subsurface plume in NEMO4. The surface freshwater runoff (the remaining 10% of the theoretical daily meltwater) is inserted into an adjacent grid cell to that used for the plume model, to simulate the portion that would remain on the surface of

281 the glacier running off from supraglacial streams. From here on, the meltwater-laced plume
282 outflow is referred to as the WB-PLUME or the EB-PLUME, which consists of >95 % seawater
283 (Fig 2. a, d).

284 The new freshwater parameterization provides a representation of glacier plume and
285 buoyancy-driven outflow within the limitations of the NEMO framework, which is not captured
286 by adding fresh, cold meltwater into the surface alone. However, entrainment of ocean waters
287 into the plume at depth is not included in NEMO, which is therefore not capturing the extent of a
288 thick, but slow inflow below the plume's neutral buoyancy (Mortensen et al., 2011). The ambient
289 ocean properties used to calculate the plume are also not coupled to the resulting plume. These
290 limitations of the modeling approach are considered in the discussion.

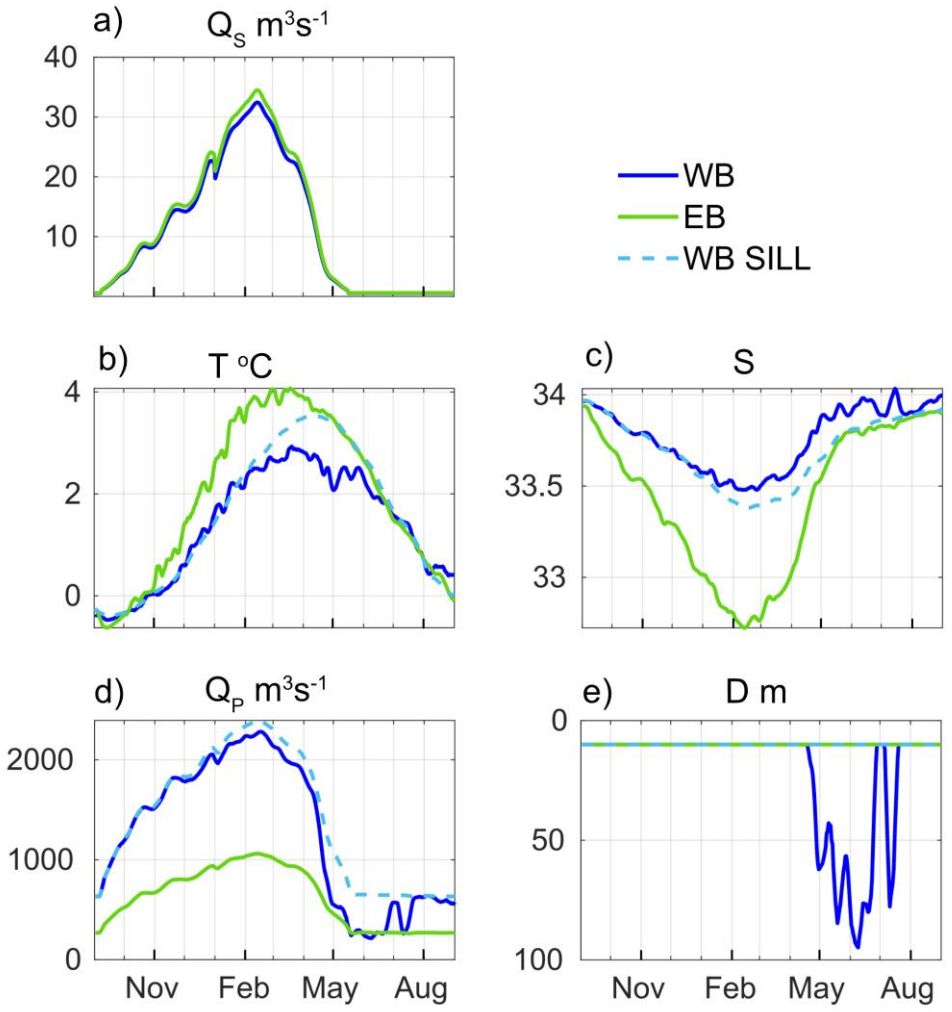

291

Figure 2. (a) The theoretical climatological cycle of meltwater discharge, Q_1, for Neumayer Glacier in WB (blue) and Nordenskjöld Glacier in EB (green) September 2005 to August 2006 (Young et al. 2011). (b) Conservative temperature, T, (c) absolute salinity, S, (d) volume, Q_2, and (e) termination depth, D, for WB-PLUME (blue) and EB-PLUME (green) in the baseline PLUME run and the for the WB-PLUME in the SILL-PLUME run (dashed blue) September 2005 to August 2006.

2.3 Model validation and run configurations

The model was validated using 11 months of CTD data collected in 2006 from the mouth of East Bay (Fig. 1b, pink star). The closest point to the mid-depth of each model level was taken from the observational data to allow direct quantitative comparison. The Root Mean Squared Error (RMSE) for conservative temperature and absolute salinity was calculated for each month of 2006 (excluding December when data were not collected) as well as the total RMSE (TRMSE). The mean near-surface error (MSE) (average of each point in the top 10 m) and mean near-bed error (MBE) (bottom model level) were calculated by subtracting observational data from model data. Finally, the Cost Function (CF) was calculated, which is a measure of model predictive skill that incorporates the standard deviation of the observational data (Holt et al., 2005). The results (Table 1) suggest that the model reproduces the observed temperature very well with the CF value well below 1 at this location. Although the CF for salinity is over 1, likely due to the timing of freshwater input (see section 3.1.1), the TRMSE is relatively small, demonstrating that this model is a useful tool for exploring the drivers of spatial and temporal variability.

	TRMSE	**MSE**	**MBE**	**CF**
T	0.39 ^{o}C	-0.04 ^{o}C	-0.24 ^{o}C	0.09
S	0.19 g/kg	-0.02 g/kg	0.01 g/kg	1.19

Table 1. Results of statistical tests from model validation.

The model is initially run from 1999-2000 to allow spin-up from initial conditions interpolated from an existing regional model (Young et al., 2016). Then the full model is run for 2000 – 2012, without the postulated sill. Process tests, which test the sensitivity of the system to individual factors, are run for September 2005 to August 2006. The baseline scenario is referred to as PLUME and the test removing WB-PLUME and EB-PLUME is referred to as NOPLUME. Inserting the shallow sill in WB and recalculating WB-PLUME and EB-PLUME via the same method as the baseline is referred to as SILL-PLUME. Inserting the sill without the WB-PLUME and EB-PLUME is referred to as SILL-NOPLUME.

3 Results

3.1 Seasonal and spatial variability

3.1.1 Temperature and salinity

The time series from the point source CTD data in 2006 reveals a strong seasonal cycle in conservative temperature (T) and absolute salinity (S) (Fig. 3). The water column is stratified in austral summer and early autumn, with the warmest surface waters between February and April due to surface heating, reaching a maximum of 4.1 ^{o}C in March, and with temperatures decreasing with depth. The water column cools in autumn and winter to a minimum of 0 ^{o}C by surface cooling and the water column is well mixed between August and October (Fig. 3a) due to mixing from winter storms. A fresh near-surface lens is observed between March and July with a minimum salinity near-surface of 32.9 in April. This is likely a combination of precipitation or the melting of floating ice, due to being a significant distance from the glaciers. Salinity increases with depth, with the greatest salinity of 34.3 near-bed between January and June, characteristic of inflowing dense shelf waters. Modeled temperature and salinity for the same location and year are largely consistent with the CTD data (Fig. 3b). The most significant difference in temperature is that the model predicts temperatures below zero (Fig. 3b). The timing of the seasonal salinity cycle is less consistent with the CTD data, with the fresh surface layer predicted ~2 months earlier than observed (Fig. 3). This may be because the theoretical melt cycle does not consider a time delay between surface heating and coastal fluxes of freshwater. In addition, as it is a climatology, it does not include the atmospheric conditions specific to 2006.

The CTD transect data from WB and EB provide some spatial context for the seasonal cycle. Hereafter, the seasonal cycle is described from spring (September) through to winter (August) and the transect CTD data from 2012, 2020, and 2021 are ordered according to season rather than year (Fig. 4). For each survey, the transect plots start from the CTD cast closest to Neumayer Glacier in West Bay and end close to Nordenskjöld Glacier in East Bay (Fig. 1b dashed grey line), with distance along the transect referenced to the central point between WB and EB mouths. In November (late spring), the warmest surface waters are at the fjord mouths and close to Neumayer Glacier (Fig. 4a). Isotherms show a complex structure, generally deepening toward the fjord mouths. Near-bed waters are slightly warmer near the mouth of

345

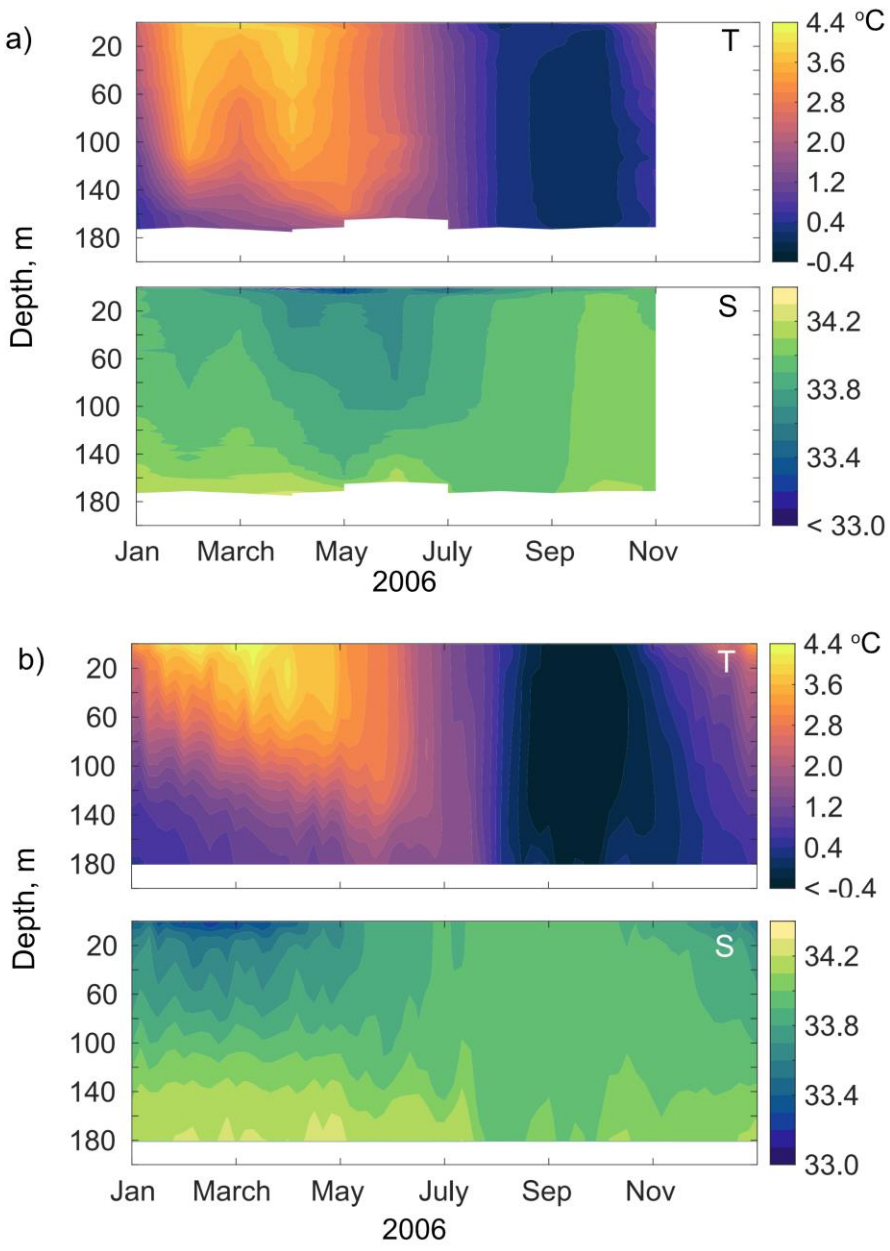

Figure 3. Conservative temperature (T) and absolute salinity (S) from (a) the CTD survey taken in the mouth of East Bay (Figure 1b, pink star) for each month, excluding December, in 2006, and (b) from the equivalent model location for each 5-day mean January to December 2006.

346

347

EB. A thin near-surface fresh lens extends along the length of WB and near Nordenskjöld Glacier in EB. Isohalines deepen steeply close to both glaciers and toward the fjord mouths. In February (late summer), there is a cold surface layer close to both Neumayer Glacier and Nordenskjöld Glacier, notably colder in WB. Below a subsurface warm layer at ~20 m, temperature decreases with depth and isotherms shallow gently toward the glaciers. Near-bed temperatures are slightly higher across the fjord mouths. The fresh surface lens observed in spring is again evident in summer, though fresher and deeper. In April (autumn), the upper ~100 m is more mixed and cooler. A thin fresh surface lens is again apparent, weaker than summer and more constrained spatially to WB mouth, and mid-way along EB.

The transects indicate that glacier processes may modify the water properties at the head of each fjord arm through cooling and freshening, particularly in summer. Near the fjord mouth, shelf-fjord exchange processes increase salinity at depth, and in spring and summer result in a near-bed intrusion of slightly warmer water. In February, the water mass properties below 25 m are very similar along the entire transect but surface waters are notably colder and fresher in WB (Fig. 5). The Temperature-Salinity (TS) lines for WB (Fig. 5, red lines) show the signature of melted glacial ice mixing with seawater; above 25 m, the lines approximately follow a melt line (grey line Fig. 5), which has a slope of roughly 2.5 ^{o}C per salinity unit (Gade slope, Gade, 1979; Mortensen et al., 2013; Straneo & Cenedese, 2015). This signature of melt could be both due to the direct melting of the submarine ice face and the submarine melting of icebergs. The change in the slope of the TS lines closer to the surface suggests that these waters are modified by a mixture of submarine melt, subglacial discharge, and surface melt, as they lie between the melt and runoff lines (Straneo & Cenedese, 2015).

The hydrographic data reveal some spatial differences between WB and EB. However, the CTD surveys do not extend close enough to Neumayer Glacier terminus to detect important differences in the glacier adjacent water column properties, and there are no data on the ocean currents. Further investigation requires analysis of the regional high-resolution ocean model.

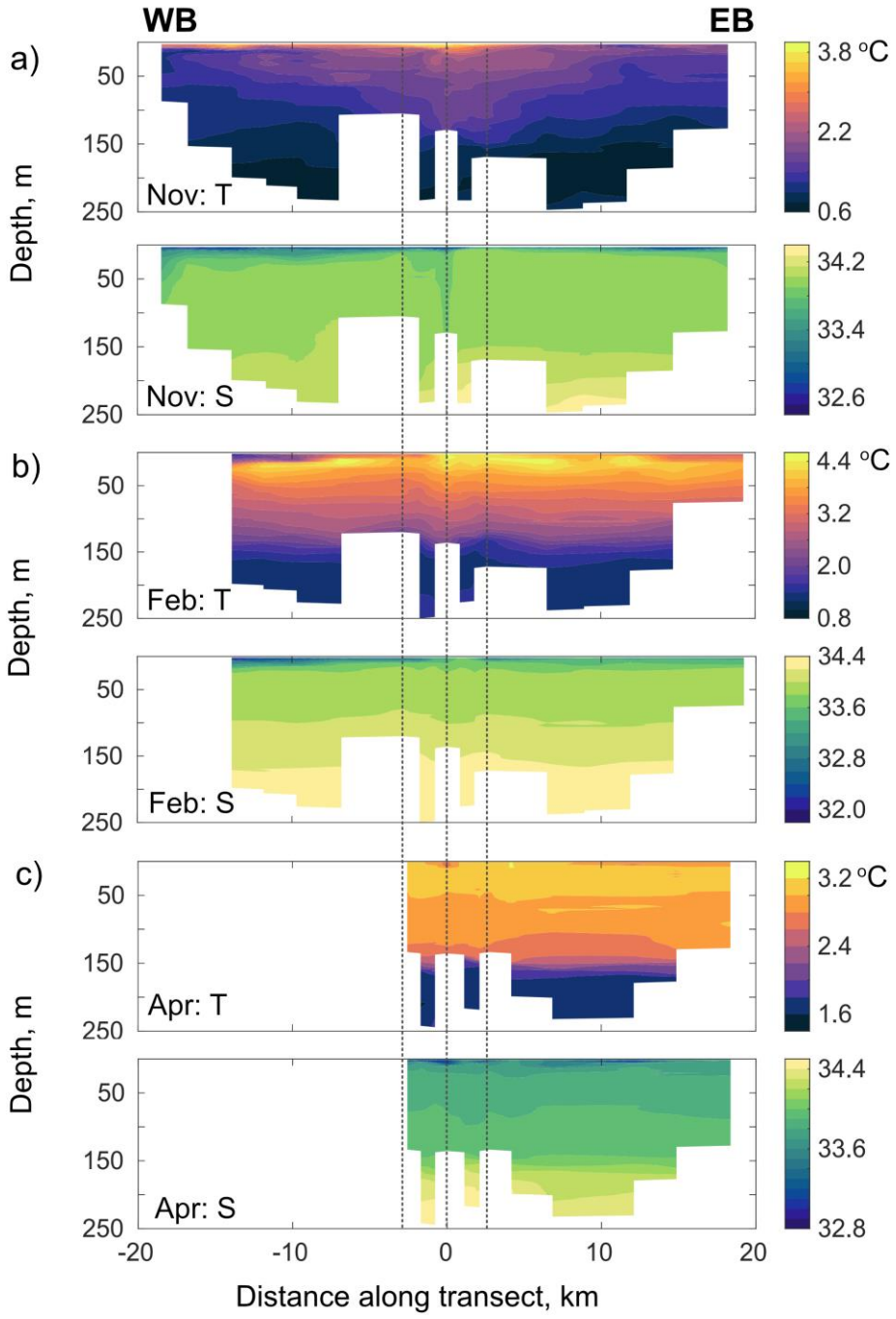

Figure 4. Transects (WB to EB; grey dashed line in Fig. 1b) of conservative temperature (T) and absolute salinity (S) for CTD surveys from (a) November 2021, (b) February 2020 and (c) April 2012. Black dashed lines indicate where the cross-mouth transects start and end. Note, the color bar scales are different for each month.

374

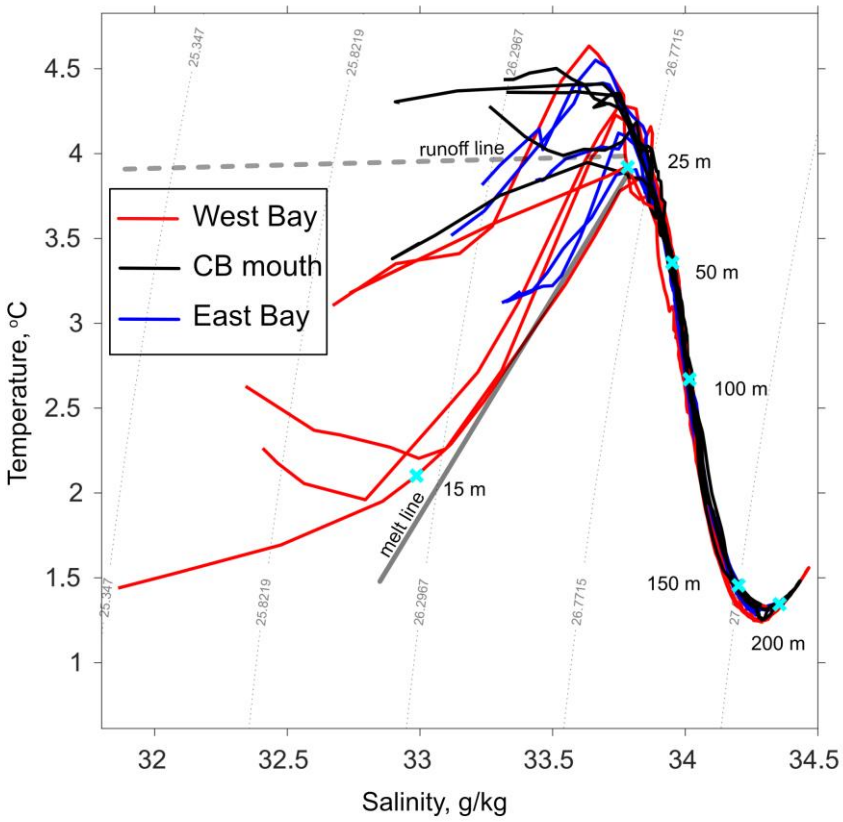

Figure 5. Temperature – salinity diagram for each CTD cast in February 2020, separated by color into West Bay transect (red), cross-mouth transect (black) and East Bay transect (blue). Isopycnals (kg/m – 1000, dotted curves), melt line (solid grey) and runoff line (dashed grey) are also shown.

3.1.2 Flow fields and sea surface temperature

A more detailed description of spatial and temporal oceanographic variability in Cumberland Bay can be gained from analysis of high-resolution model output, here focusing on near-surface flows, depth-averaged flows and sea surface temperatures (SST) (Fig. 6). The seasonal variability is illustrated with monthly averages for November (spring), February (summer), May (autumn), and August (winter).

The surface (top model layer) currents show largely the same pattern as the depth-averaged currents for each month (Fig. 6). In spring and summer there is enhanced flow along the north coast of WB and the east coast of EB which crosses to the west coast at the mouth, and is subsequently entrained into the stronger northwestward shelf flows (Fig. 6). The Rossby radius of deformation is larger than the narrow fjord width, so cross-fjord variations are not induced by the Coriolis force (Cottier et al., 2010). The baroclinic surface flows are strongest in summer when the volume of meltwater runoff, and therefore buoyancy-driven outflow, is greatest (Fig. 2a) which is inferred by the greatest difference between the surface and depth-averaged flows (Fig. 6). Surface flows weaken in May, as meltwater runoff reduces steeply (Fig. 2a). Winter storms drive mixing which weakens the stratification allowing bathymetric steering of coastal flows into the fjord mouth. The buoyancy-driven outflow is no longer the dominant driver of circulation in winter, reflecting the seasonality of freshwater forcing.

The sea surface temperature (SST) is cold in spring (~0 ^{o}C), coldest in the tributary fjords and at the head of WB (Fig. 6). The SST warms significantly in summer and autumn (~3-4 ^{o}C) though notably colder in WB compared to EB. The colder surface waters in WB are consistent with the colder properties of WB-PLUME compared to EB-PLUME (Fig. 2b). In winter, the SST is similar between the fjord arms, consistent with the lower volume of the WB- and EB-PLUME and buoyancy-driven outflow no longer being a dominant driver of circulation.

While many aspects of seasonal variability are not yet verified, the model provides a useful tool for testing hypotheses. Variability in shelf-fjord exchange, apparent in the flow fields and near-bed water properties, and the interaction of such flows with the fjord outer sills, will contribute to temporal and spatial variability at the fjord mouths, however, this is beyond the scope of the present study. Instead, based on the clear influence of glacial meltwater in the observations, we focus on the role of buoyancy-driven outflow in driving spatial and temporal

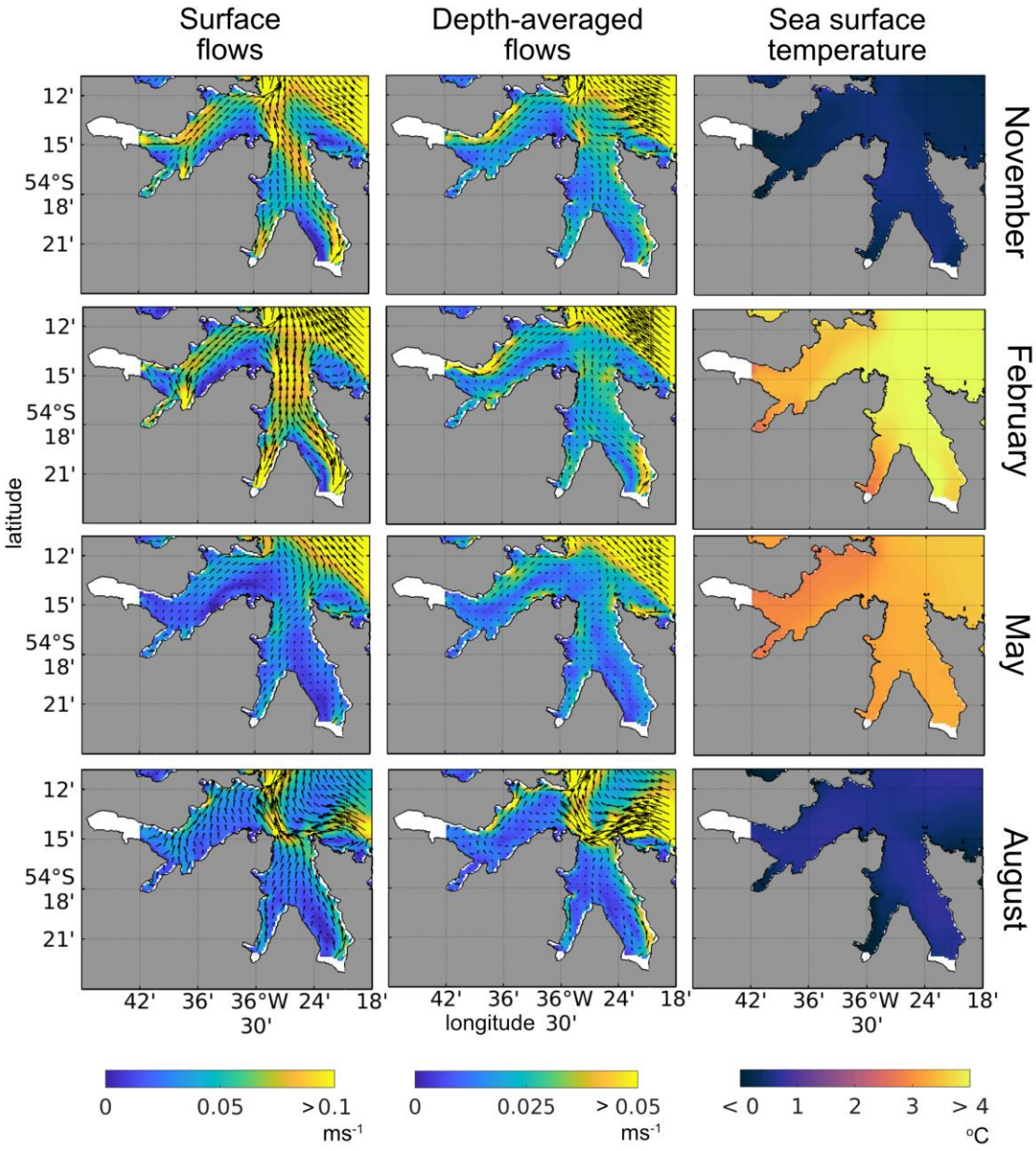

409

Figure 6. Surface flow, depth-averaged flow, and sea surface temperature, averaged over the months of November, February, May, and August. Note the difference in color scale between the surface and depth-averaged flows.

variability close to Neumayer and Nordenskjöld Glaciers and we concentrate further model analyses on this region.

3.2 Drivers of variability

3.2.1 Buoyancy-driven outflow

Volume transport through cross-sections ~1 km from Neumayer and Nordenskjöld Glaciers show a distinct difference in circulation patterns between the two fjord arms (Fig. 7, locations of cross-sections in Fig. 1c, red dashes). In WB, the average volume transport in November shows a 4-layer structure from the surface to the bed of alternating outflow and inflow. In February, when the volume of WB-PLUME is greatest (Fig. 2d), there is strong outflow in the north, with weaker inflow in the south in the upper ~60 m. The outflow in the north becomes a subsurface feature in May with surface inflow across the width of WB; this coincides with a sharp reduction in WB-PLUME volume and the onset of subsurface WB-PLUME termination (Fig. 2e). In August, following a period of low WB-PLUME volume, the structure reduces to 2 layers with surface outflow and inflow below ~50 m. In November in EB, there is a predominant 2-layer structure of surface inflow and outflow at depth in the west, with the reverse structure in the east (Fig. 7b). This pattern continues largely unchanged in February and May, before a distinct shift in August to inflow in the west and outflow in the east (Fig. 7b), due to more barotropic flows in the destratified water column (Fig. 3). The EB-PLUME is confined to the upper 20 m, increasing the strength of the surface outflow in spring and summer in line with the near-surface flows (Fig. 6).

To test the influence of the WB- and EB-PLUME on the circulation patterns, we compare directly to the NOPLUME scenario. The total volume transport through each section was integrated across the fjord width and averaged over 30-day intervals to enable visualization of the seasonal cycle in transport variability with and without the plume (Fig. 8). In WB, the thick surface outflow that moves subsurface between April and July is clearly a response to the WB-PLUME; with NOPLUME there is a thin surface outflow and subsurface inflow between ~10 and 50 m throughout the year (Fig. 8a). In EB, outflow is confined to the upper ~20 m for the majority of the year with EB-PLUME, becoming thicker and weaker in winter. With NOPLUME the transport pattern remains the same, but with weaker surface outflow (Fig. 8b).

440

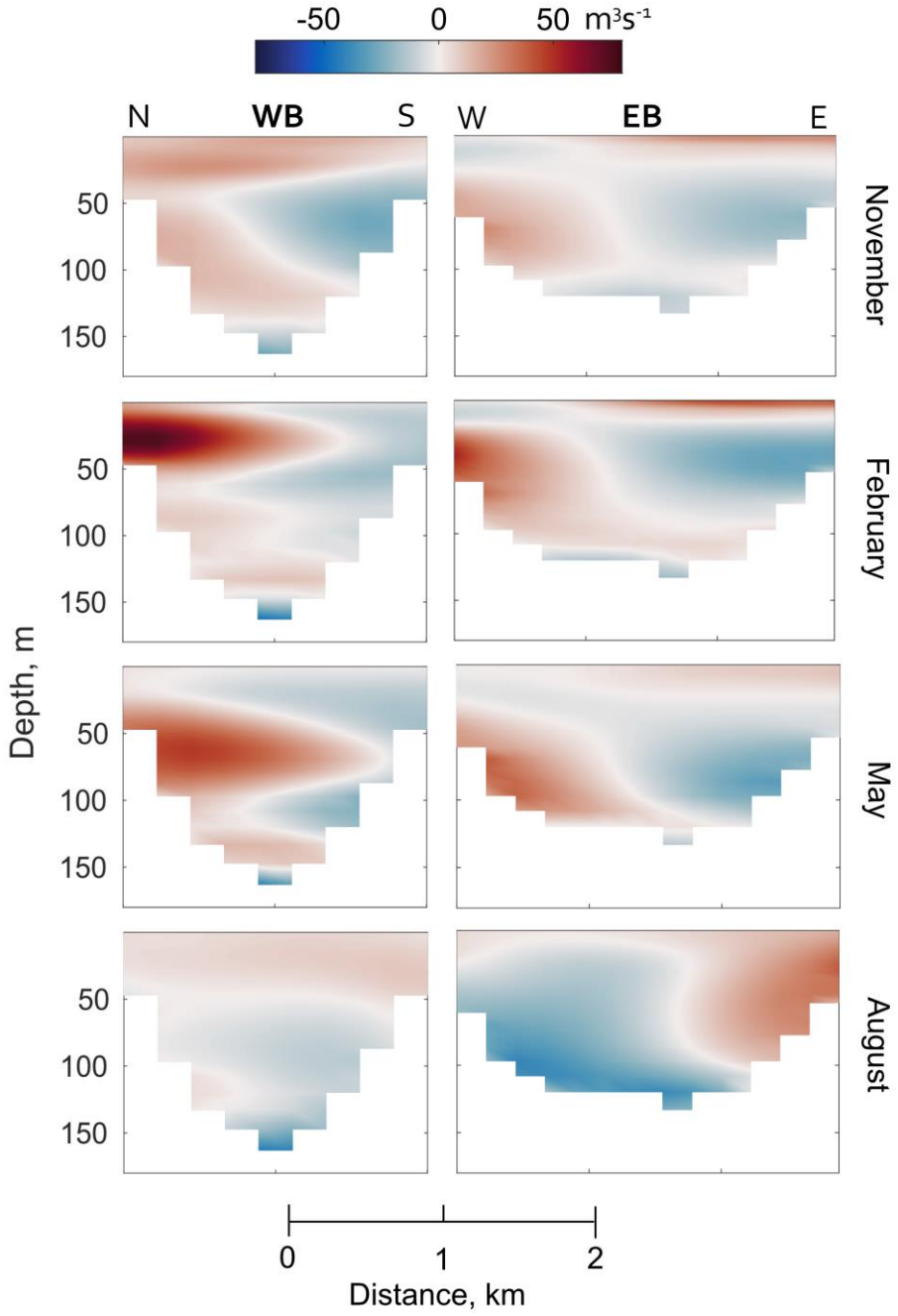

Figure 7. Monthly-averaged volume transport through cross-sections ~1 km from Neumayer Glacier (WB, north (N) to south (S)) and Nordenskjöld Glacier (EB, west (W) to east (E)) (Fig. 1c, red dashed lines). Red indicates outflow, toward the fjord mouth, and blue indicates inflow, toward the glaciers.

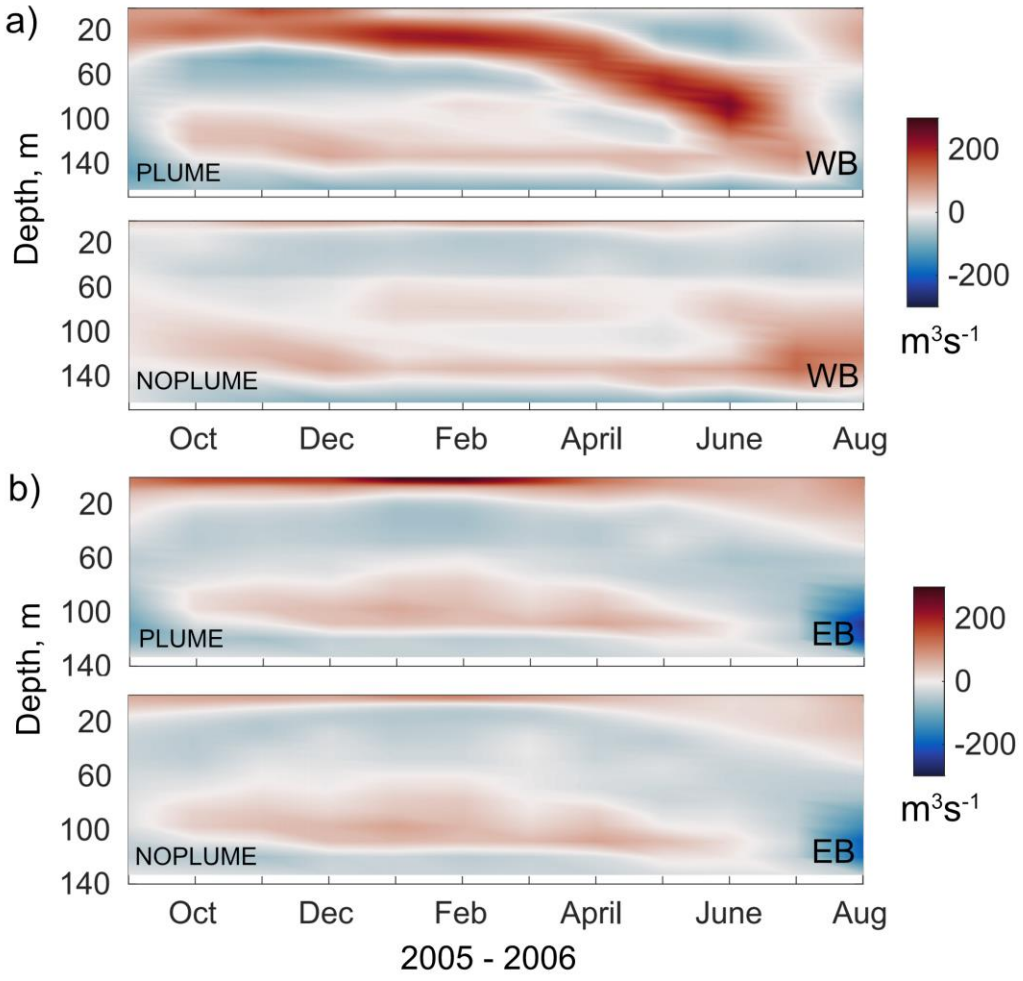

441

Figure 8. Monthly-averaged volume transport integrated across model levels through cross-sections ~1 km from (a) Neumayer Glacier (WB) and (b) Nordenskjold Glacier (EB) (red dashed lines in Fig. 1c), comparing PLUME and NOPLUME model runs; September 2005 to August 2006.

442

443

444 The buoyancy-driven outflow from WB-PLUME and EB-PLUME drive distinctly
445 different circulation patterns for much of the year (Fig. 8). One key difference between WB and
446 EB underlying this disparity is the seabed depth adjacent to the glaciers. WB is deeper, hence the
447 water properties used to calculate WB-PLUME are colder and more saline relative to those in
448 EB (Fig. 2) and this is reflected in the SST (Fig. 6). The outflow of WB-PLUME is greater and
449 spread over a larger depth in WB compared to EB. Due to the volume of subglacial discharge
450 and the properties of the water in autumn, the plume in WB terminates below the surface, driving
451 a different circulation pattern at this time of year (Fig. 7). These results strongly suggest the
452 subglacial plume is an important feature, and the plume dynamics are sensitive to the relatively
453 small depth range of these shallow glaciers. The model simulations demonstrate that the glacial
454 plumes have a significant impact on patterns of circulation in WB and EB, and it is possible the
455 retreat rates of Neumayer and Nordenskjöld Glacier are sensitive to the small differences in
456 oceanography. However, a perhaps more significant driver of spatial differences in
457 oceanography is the postulated inner sill in WB.

458 **3.2.2 West Bay postulated inner sill**

459 The model simulation was repeated with an inner sill artificially inserted in WB as barrier
460 1-grid cell wide and sitting at 30 m below the sea surface (Fig. 9a, location in Fig. 1c white
461 dashed line) (SILL-PLUME) to test the impact of the postulated WB inner sill on the
462 oceanography. Analysis of water properties in April for a transect along the center of WB shows
463 the new inner basin to be warmer, fresher, and well-mixed compared to the outer basin (Fig. 9a).
464 The near-bed temperature in the center of the inner basin is ~2 ^{o}C higher than the comparable
465 PLUME run (Fig. 9b). Higher near-bed temperatures are also predicted by the SILL-NOPLUME
466 simulation (Fig. 9b), which shows that the sill is the underlying driver in both cases. Warmer,
467 fresher surface waters from the outer basin flow over the sill, where they are mixed, while deeper
468 waters are blocked by the sill, leading to near uniform T and S in the inner basin (Fig. 9a),
469 similar to observed processes over transverse ridges on the West Antarctic Peninsula shelf
470 (Venables et al., 2017). With no sill present, WB-PLUME decreases the near-surface
471 temperature in summer and autumn (Fig. 9b, blue lines). For the SILL-PLUME scenario, WB-
472 PLUME decreases the near-surface temperature in summer and slightly increases the near-
473 surface temperature in autumn (Fig. 9b, red lines). Therefore, the presence of the sill affects the

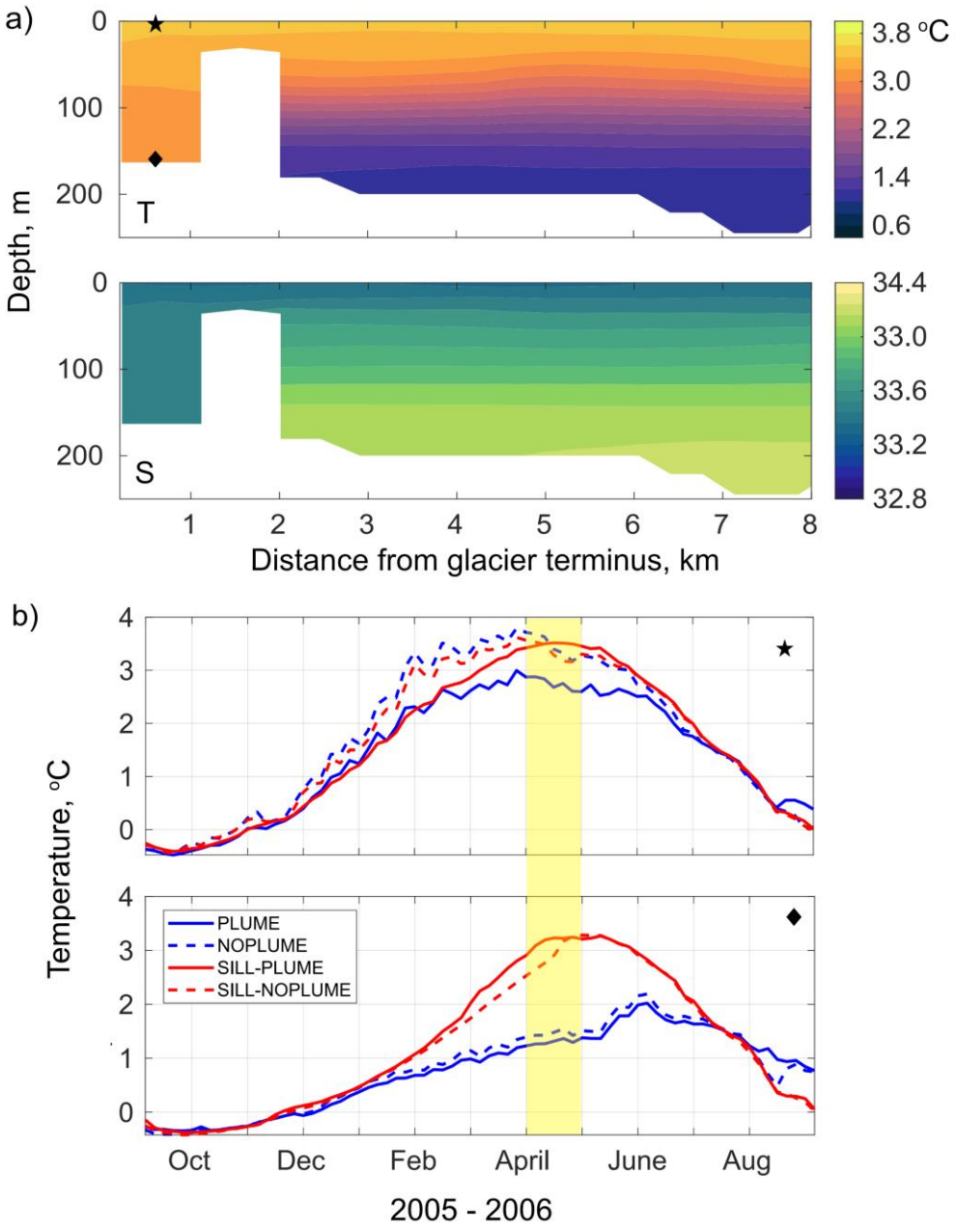

Figure 9. (a) Monthly averaged (April 2006) conservative temperature (T) and absolute salinity (S) from the SILL-PLUME model run for an 8 km transect along the centre of WB from Neumayer Glacier terminus. (b) 5-day mean near-surface (star in panel (a)) and near-bed (diamond in panel (a)) temperatures for September 2005 to August 2006, from the four model runs defined in the legend. The month of April is highlighted in yellow.

full water column near the glacier, but the most significant changes are near-bed with the increase in temperature, which may have implications for glacier retreat.

The integrated volume transport through the WB section was calculated for the SILL-PLUME and SILL-NOPLUME simulations for comparison with the results described in section 3.3. The transport patterns through the section, which now lies within the inner basin, show that when a sill is present the buoyancy-driven outflow drives a different circulation pattern (Fig. 10). The SILL-PLUME simulation predicts a thick surface outflow throughout the year in the upper ~50 m, deepening in winter, and inflow between ~50 and 100 m from spring to early autumn. Below ~100 m there is relatively low volume transport in spring and summer, and a strong inflow in autumn and winter. Compared with the SILL-NOPLUME run, it is apparent that the WB-PLUME is driving the pattern of strong outflow overlying inflow in spring and summer, and extending the duration of near-bed inflow in autumn and winter. As the peak of the sill is 30 m below the sea surface, a portion of the buoyancy-driven outflow flows over the sill, but below 30 m the outflow is blocked by the sill and re-circulates as subsurface inflow. Warmer surface waters from the outer basin flow into the inner basin over the sill along the south coast in the spring and summer (not shown), but integrating the volume transport along model levels masks this cross-fjord variability as the outflow from the plume dominates. In winter, as the volume of the WB-PLUME lessens and the density in the outer basin increases (temperatures cool and salinity increases, Fig. 3), waters from the outer basin encroach into the inner basin, sink, and present as a strong inflow at depth (Fig. 10).

An important difference between the model runs with and without an inner sill is that the PLUME run no longer has a sub-surface terminating plume for a portion of the year in WB (Fig. 2e). Due to the now uniform density within the inner basin resulting from the sill, the plume, derived from SILL-NOPLUME, does not reach any neutral density before the surface at any time of the year.

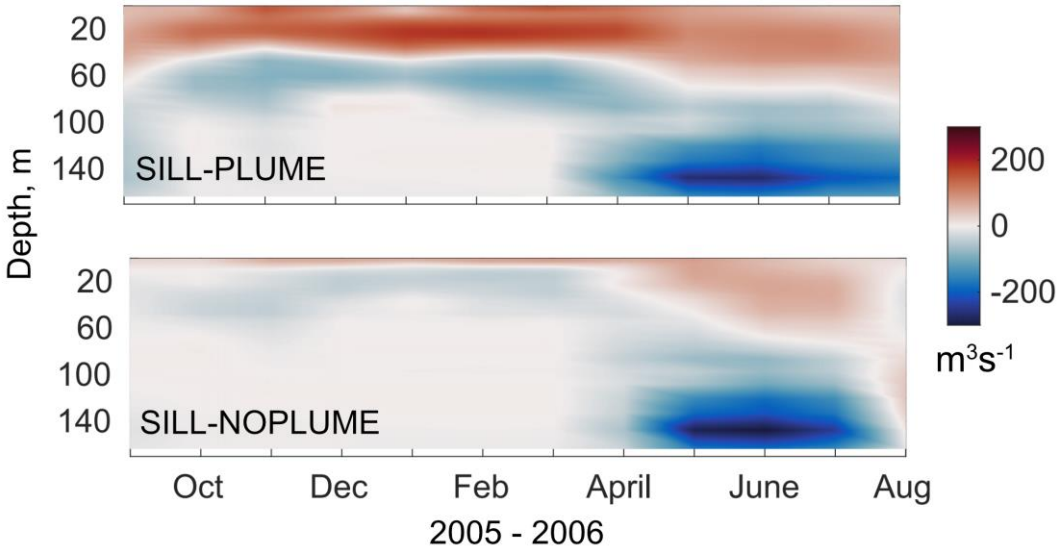

Figure 10. Monthly averaged volume transport integrated across model levels though the cross-section in WB (red dashed line Fig. 1c) for the SILL-PLUME and SILL-NOPLUME model runs; September 2005 to August 2006 Red indicates transport toward the fjord mouth, and blue indicates transport toward the Neumayer Glacier terminus.

4 Discussion

4.1 Oceanographic variability and modeling limitations

The oceanographic data presented and analysed in this study provide valuable information on the hydrography of Cumberland Bay. Freshwater signals are apparent in the data, but whether this can be attributed to surface meltwater runoff, subglacial discharge, melting of ice mélange, or increased precipitation is not completely clear. The cold, fresh signature of meltwater emerging as subglacial discharge may not be retained due to plume entrainment, meaning this can be hard to identify in the CTD data (Carroll et al., 2015). The oceanographic data reveal a strong seasonal cycle likely due to the combined effects of freshwater forcing,

shelf-fjord exchange, and atmospheric forcing (particularly winds). However, the temporal and spatial limitations of the observational data hinder a more detailed analysis.

With the use of the new high-resolution oceanographic model, we identified that freshwater forcing, which is dominated by subglacial discharge at the two main glaciers at the heads of WB and EB, is a key driver of spatial variability in spring through to autumn. This is due to the seasonal cycle of subglacial meltwater input and the bathymetric differences between the fjord arms. Wind forcing and fjord-shelf exchange likely dominates the spatial variability in flows in winter and are the focus of ongoing research.

The addition of an inner sill in WB has a significant impact on the simulated seasonal and spatial variability and has implications for the retreat of Neumayer Glacier, discussed further below. Neither scenario can yet be considered a more accurate representation of WB as the true bathymetry and the extent of the sill are unknown. However, the results clearly identify the sensitivity of the fjord oceanography to bathymetry and geometric controls on the circulation regime and suggest that buoyancy-driven circulation is likely to have varied considerably at different stages of past glacier front positions.

Though the model provides useful insights, the caveats must be considered. It is stressed that the plume dynamics and ocean model are not coupled, which limits the interpretation of the results. The ambient water column entrained in the offline plume model is unmodified by freshwater forcing, and the circulation resulting from entrainment into the plume is not captured, suggesting the ocean model may be underrepresenting inflow at depth. The implications of this are difficult to infer without the use of a coupled model. Additionally, the melting of icebergs is not represented in the model but is likely to have some influence on the hydrography (Fig. 5) and circulation (Davison et al., 2020). Despite these limitations, this study provides valuable insights into the oceanographic variability in Cumberland Bay, while emphasizing the importance of representing plume dynamics for the simulation of circulation in fjords with marine-terminating glaciers.

4.2 Implications for glacier retreat

Neumayer Glacier in WB has retreated far quicker than Nordenskjöld Glacier in EB but the drivers of this differential retreat rate are currently unknown. We hypothesize here that

changes to water column properties adjacent to Neumayer Glacier due to a postulated shallow inner sill in WB are playing a key role in the differential retreat rate.

The results of model experiments show that the presence of a bathymetric barrier representing the inner sill blocks colder waters at depth, resulting in a warmer, well-mixed inner basin (Fig. 9a). This warmer water in the vicinity of the glacier terminus can be inferred to increase glacier melt, and even potentially drive a positive feedback mechanism that would further increase glacial retreat from the sill, although as there is no ice-plume-ocean coupling in the model, such implications remain speculative. Assuming the melt rate is proportional to the thermal driving multiplied by the boundary layer velocity (Bradley et al., 2022; Millgate et al., 2013), it is informative to examine the modeled glacier-adjacent temperatures and (ice-tangential) horizontal velocities, not including velocities associated with the vertical plume (Fig. 11.) We find that temperatures are increased on average over summer and autumn (6 months) with a sill present (SILL-PLUME) (Fig. 11). Horizontal speeds are similar between PLUME and SILL-PLUME scenarios, though there is an indication of higher horizontal speeds towards the south of Neumayer Glacier face. With no sill present, WB-PLUME decreases the water temperature adjacent to the glacier, whereas with a sill present WB-PLUME very slightly increases the water temperature near-bed (Fig. 11). We can reasonably infer that melt rates are likely to be higher for SILL-PLUME than PLUME due to the warmer waters (increased thermal driving) adjacent to the glacier submarine face. In fact, the offline plume model predicts melt rates ~1 m/day greater in late summer/early autumn with the SILL-PLUME scenario within the vicinity of the theoretical plume, compared to the PLUME scenario (not shown). Therefore, the observed rapid retreat of Neumayer Glacier may be the consequence of a positive feedback, whereby warmer water is trapped and recirculated in the inner basin, promoting higher submarine melt rates through increased thermal driving. Increased submarine melting will both increase turbulence and reduce the density of the inner basin, driving a stronger inflow of warmer waters, thus promoting further melting through both increased ice-face boundary layer velocities and thermal driving. Additionally, warmer waters at depth may promote undercutting, which could lead to greater mass loss through calving (Benn et al., 2017). Interpretation of the results requires caution as the plume would also introduce high vertical velocities not captured in the ocean model, as well as increase the horizontal velocities regardless of the presence of a sill. The processes described here, and the proposed positive feedback mechanism, are not

present in EB as the inner sill peak is much deeper. This might explain why Nordenskjöld Glacier has remained relatively stable in the presence of oceanic variability that is apparently uniform across the two fjord arms.

The hypothesis of a positive feedback mechanism involving an inner sill is supported by observations of the front positions of Neumayer Glacier. The terminus stayed relatively stable in the vicinity of the postulated sill between 1955 and 1989, followed by rapid retreat once the

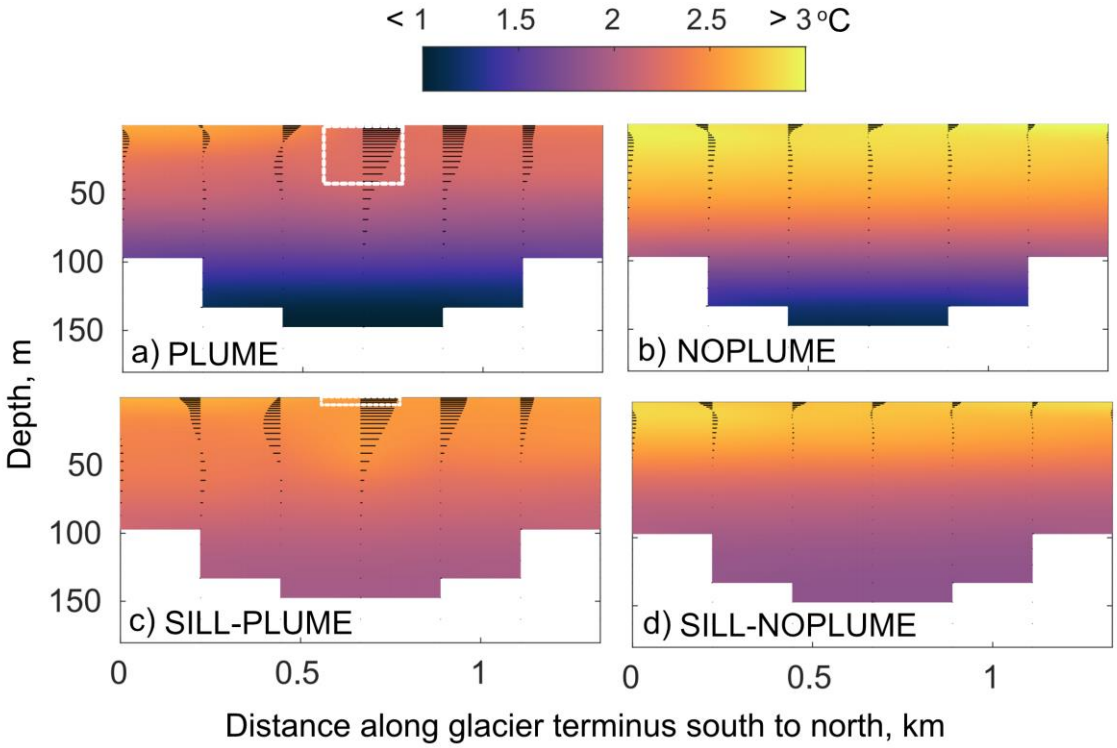

Figure 11. 6-month average (December 2005 to May 2006) of conservative temperature (shading) and horizontal velocities (black lines) adjacent to Neumayer Glacier, drawn facing the glacier terminus for (a) PLUME, (b) NOPLUME, (c) SILL-PLUME and (d) SILL-NOPLUME. The largest area over which WB-PLUME is inserted during this time period is highlighted by the white dashed boxes in (a) and (c).

glacier had moved behind the sill (Cook et al., 2010). However, it remains unclear what caused Neumayer Glacier to retreat past the sill in the first instance. Further exploration of this hypothesis requires a more comprehensive study, including detailed bathymetric surveys of the head of WB up to Neumayer Glacier terminus and a more accurate model representation of the WB inner sill. Future modeling work could be greatly enhanced by the development of an ice-ocean-atmosphere coupled model at higher spatial resolution.

In previous studies focused on Greenland fjords, the presence of a shallow sill has been shown to reduce the melting of tidewater glaciers due to colder waters overlaying warmer waters (Millan et al., 2018; Schaffer et al., 2020). We find that in fjord systems where warmer waters overlay colder waters the opposite holds and a shallow sill may promote higher melt rates.

5 Conclusions

This study combines observational data and a new high-resolution validated model of Cumberland Bay, South Georgia, to greatly improve the understanding of the oceanographic variability and the drivers of glacier retreat. Results show that the seasonal cycle is strongly influenced by freshwater forcing via subglacial plumes. The difference in bathymetry between Cumberland Bay's two fjord arms, West Bay and East Bay, results in differing signals of buoyancy-driven outflow. The possible presence of an inner sill in West Bay alters the seasonal variability in buoyancy-driven outflow and the properties within the inner basin. We find evidence to suggest that the rapid retreat of Neumayer Glacier in West Bay, compared to Nordenskjöld Glacier in East Bay, might be explained by the trapping of warmer waters adjacent to the glacier by a postulated inner sill, with a possible positive feedback mechanism enhancing glacial melt. Further study is required to test this hypothesis, through the acquisition of accurate bathymetric data over the sill in West Bay together with a coupled ice-ocean-atmosphere model at higher resolution. With the use of the new model as a tool, future studies can identify other key drivers of variability in circulation and shelf exchange, as well as investigate interannual variability that may have triggered the retreat.

The fjord circulation patterns identified in this study have wider implications beyond glacier retreat. For example, the seasonality of buoyancy-driven outflow and the cross-fjord flow

variability suggest the transport and retention of fish larvae will be sensitive to the timing and location of egg hatching. The availability of iron for downstream phytoplankton blooms derived from glacial flour plumes may be limited by a subsurface terminating plume or the presence of a sill acting as a barrier. This study is a fundamental step toward understanding the implications of oceanographic variability for glacier dynamics in Cumberland Bay, whilst providing a tool for investigating the impact of oceanographic variability on the marine ecosystem at South Georgia.

Acknowledgments

This work was supported by the Natural Environment Research Council via the BAS Polar Oceans program and the INSPIRE Doctoral Training Partnership. The authors would like to thank Polar Seafish Ltd for additional support and funding. We thank the Government of South Georgia and the South Sandwich Islands and the crew of the Pharos SG for facilitating and aiding CTD data collection. The numerical simulations were carried out on the ARCHER2 UK National Supercomputing Service (https://www.archer2.ac.uk/).

Data availability statement

The data are currently available in the provided figures and tables. The observational data and model output underlying the figures and tables in this paper are in the process of being made available through the UK Polar Data Centre. The model code for NEMO-4.0.6 is available from the NEMO website (**www.nemo-ocean.eu**).

631

632 **References**

633 Bartholomaus, T. C., Stearns, L. A., Sutherland, D. A., Shroyer, E. L., Nash, J. D., Walker, R. T.,
634 Catania, G., Felikson, D., Carroll, D., Fried, M. J., Noël, B. P. Y., & van den Broeke, M. R.
635 (2016). Contrasts in the response of adjacent fjords and glaciers to ice-sheet surface melt in
636 West Greenland. *Annals of Glaciology*, *57*(73), 25–38. https://doi.org/10.1017/aog.2016.19

637 Benn, D. I., Cowton, T., Todd, J., & Luckman, A. (2017). Glacier Calving in Greenland. In
638 *Current Climate Change Reports* (Vol. 3, Issue 4). https://doi.org/10.1007/s40641-017-
639 0070-1

640 Berntsen, J., Xing, J., & Davies, A. M. (2009). *Numerical studies of flow over a sill : sensitivity*
641 *of the non-hydrostatic effects to the grid size*. 1043–1059. https://doi.org/10.1007/s10236-
642 009-0227-0

643 Boone, W., Rysgaard, S., Kirillov, S., Dmitrenko, I., Bendtsen, J., Mortensen, J., Meire, L.,
644 Petrusevich, V., & Barber, D. G. (2017). Circulation and fjord-shelf exchange during the
645 ice-covered period in Young Sound-Tyrolerfjord, Northeast Greenland (74°N). *Estuarine,*
646 *Coastal and Shelf Science*, *194*, 205–216. https://doi.org/10.1016/j.ecss.2017.06.021

647 Bradley, A. T., Bett, D. T., Dutrieux, P., de Rydt, J., & Holland, P. R. (2022). The Influence of
648 Pine Island Ice Shelf Calving on Basal Melting. *Journal of Geophysical Research: Oceans*,
649 *127*(9). https://doi.org/10.1029/2022JC018621

650 Carroll, D., Sutherland, D. A., Shroyer, E. L., Nash, J. D., Catania, G. A., & Stearns, L. A.
651 (2015). Modeling turbulent subglacial meltwater plumes: Implications for fjord-scale
652 buoyancy-driven circulation. *Journal of Physical Oceanography*.
653 https://doi.org/10.1175/JPO-D-15-0033.1

654 Catania, G. A., Stearns, L. A., Sutherland, D. A., Fried, M. J., Bartholomaus, T. C., Morlighem,
655 M., Shroyer, E., & Nash, J. (2018). Geometric Controls on Tidewater Glacier Retreat in
656 Central Western Greenland. *Journal of Geophysical Research: Earth Surface*, *123*(8),
657 2024–2038. https://doi.org/10.1029/2017JF004499

Christoffersen, P., Mugford, R. I., Heywood, K. J., Joughin, I., Dowdeswell, J. A., Syvitski, J. P. M., Luckman, A., & Benham, T. J. (2011). Warming of waters in an East Greenland fjord prior to glacier retreat: Mechanisms and connection to large-scale atmospheric conditions. *Cryosphere*. https://doi.org/10.5194/tc-5-701-2011

Chu, V. W. (2014). Greenland ice sheet hydrology: A review. *Progress in Physical Geography*, *38*(1). https://doi.org/10.1177/0309133313507075

Cook, A. J., Poncet, S., Cooper, A. P. R., Herbert, D. J., & Christie, D. (2010). Glacier retreat on South Georgia and implications for the spread of rats. *Antarctic Science*, *22*(3), 255–263. https://doi.org/10.1017/S0954102010000064

Cottier, F. R., Nilsen, F., Skogseth, R., Tverberg, V., Skardhamar, J., & Svendsen, H. (2010). Arctic fjords: A review of the oceanographic environment and dominant physical processes. *Geological Society Special Publication*, *344*(November), 35–50. https://doi.org/10.1144/SP344.4

Cowton, T., Slater, D., Sole, A., Goldberg, D., & Nienow, P. (2015). Modeling the impact of glacial runoff on fjord circulation and submarine melt rate using a new subgrid-scale parameterization for glacial plumes. *Journal of Geophysical Research: Oceans*. https://doi.org/10.1002/2014JC010324

DAVIES, H. (1976). A lateral boundary formulation for multi-level prediction models. *Quarterly Journal of the Royal Meteorological Society*, *102*(432). https://doi.org/10.1256/smsqj.43209

Davison, B. J., Cowton, T. R., Cottier, F. R., & Sole, A. J. (2020). Iceberg melting substantially modifies oceanic heat flux towards a major Greenlandic tidewater glacier. *Nature Communications*, *11*(1). https://doi.org/10.1038/s41467-020-19805-7

Egbert, G. D., & Erofeeva, S. Y. (2002). Efficient inverse modeling of barotropic ocean tides. *Journal of Atmospheric and Oceanic Technology*. https://doi.org/10.1175/1520-0426(2002)019<0183:EIMOBO>2.0.CO;2

ENGEDAHL, H. (1995). Use of the flow relaxation scheme in a three-dimensional baroclinic ocean model with realistic topography. *Tellus A*, *47*(3). https://doi.org/10.1034/j.1600-0870.1995.t01-2-00006.x

686 Everson, I. (1992). Managing Southern Ocean krill and fish stocks in a changing
687 environment. *Philosophical Transactions - Royal Society of London, B*, *338*(1285), 311–
688 317. https://doi.org/10.1098/rstb.1992.0151

689 Everson, I., North, A. W., Paul, A., Cooper, R., McWilliam, N. C., & Kock, K. H. (2001).
690 Spawning locations of mackerel icefish at South Georgia. *CCAMLR Science*.

691 Flather, R. A. (1994). A storm surge prediction model for the northern Bay of Bengal with
692 application to the cyclone disaster in April 1991. *Journal of Physical Oceanography*, *24*(1).
693 https://doi.org/10.1175/1520-0485(1994)024<0172:ASSPMF>2.0.CO;2

694 Fraser, N. J., & Inall, M. E. (2018). Influence of Barrier Wind Forcing on Heat Delivery Toward
695 the Greenland Ice Sheet. *Journal of Geophysical Research: Oceans*, *123*(4), 2513–2538.
696 https://doi.org/10.1002/2017JC013464

697 Gade, H. G. (1979). Melting of Ice in Sea Water: A Primitive Model with Application to the
698 Antarctic Ice Shelf and Icebergs. *Journal of Physical Oceanography*, *9*(1).
699 https://doi.org/10.1175/1520-0485(1979)009<0189:moiisw>2.0.co;2

700 Gordon, J. E., Haynes, V. M., & Hubbard, A. (2008). Recent glacier changes and climate trends
701 on South Georgia. *Global and Planetary Change*, *60*(1–2), 72–84.
702 https://doi.org/10.1016/j.gloplacha.2006.07.037

703 Hager, A. O., Sutherland, D. A., Amundson, J. M., Jackson, R. H., Kienholz, C., Motyka, R. J.,
704 & Nash, J. D. (2022). Subglacial Discharge Reflux and Buoyancy Forcing Drive
705 Seasonality in a Silled Glacial Fjord. *Journal of Geophysical Research: Oceans*, *127*(5).
706 https://doi.org/10.1029/2021JC018355

707 Hersbach, H., Bell, B., Berrisford, P., Hirahara, S., Horányi, A., Muñoz-Sabater, J., Nicolas, J.,
708 Peubey, C., Radu, R., Schepers, D., Simmons, A., Soci, C., Abdalla, S., Abellan, X.,
709 Balsamo, G., Bechtold, P., Biavati, G., Bidlot, J., Bonavita, M., … Thépaut, J. N. (2020).
710 The ERA5 global reanalysis. *Quarterly Journal of the Royal Meteorological Society*,
711 *146*(730). https://doi.org/10.1002/qj.3803

712 Hewitt, I. J. (2020). Subglacial Plumes. *Annual Review of Fluid Mechanics*, *52*(1), 145–169.
713 https://doi.org/10.1146/annurev-fluid-010719-060252

Hodgson, D. A., Graham, A. G. C., Grif, H. J., Roberts, S. J., Cofaigh, C. Ó., Bentley, M. J., & Evans, D. J. A. (2014). *Glacial history of sub-Antarctic South Georgia based on the submarine geomorphology of its fjords q*. *89*, 129–147. https://doi.org/10.1016/j.quascirev.2013.12.005

Hogg, O. T., Huvenne, V. A. I., Griffiths, H. J., Dorschel, B., & Linse, K. (2016). Landscape mapping at sub-Antarctic South Georgia provides a protocol for underpinning large-scale marine protected areas. *Scientific Reports*, *6*. https://doi.org/10.1038/srep33163

Holland, D. M., & Jenkins, A. (1999). Modeling thermodynamic ice-ocean interactions at the base of an ice shelf. *Journal of Physical Oceanography*, *29*(8 PART 1). https://doi.org/10.1175/1520-0485(1999)029<1787:mtioia>2.0.co;2

Hollingsworth, A., Kållberg, P., Renner, V., & Burridge, D. M. (1983). An internal symmetric computational instability. *Quarterly Journal of the Royal Meteorological Society*, *109*(460). https://doi.org/10.1002/qj.49710946012

Holmes, T. M., Wuttig, K., Chase, Z., Schallenberg, C., van der Merwe, P., Townsend, A. T., & Bowie, A. R. (2019). Glacial and hydrothermal sources of dissolved iron(II) in Southern Ocean waters surrounding Heard and McDonald Islands. In *In Prep.* (Issue Ii). https://doi.org/10.1029/2020JC016286

Holt, J. T., Allen, J. I., Proctor, R., & Gilbert, F. (2005). Error quantification of a high-resolution coupled hydrodynamic-ecosystem coastal-ocean model: Part 1 model overview and assessment of the hydrodynamics. *Journal of Marine Systems*, *57*(1–2). https://doi.org/10.1016/j.jmarsys.2005.04.008

Jenkins, A. (2011). Convection-driven melting near the grounding lines of ice shelves and tidewater glaciers. *Journal of Physical Oceanography*. https://doi.org/10.1175/JPO-D-11-03.1

Large, W. G., & Yeager, S. G. (2004). Diurnal to decadal global forcing for ocean and sea-ice models: the data sets and flux climatologies. *Ech. Rep., NCAR Climate and Global Dynamics Division; Boulder, CO, United States*.

741 Lin, P., Pickart, R. S., Torres, D. J., & Pacini, A. (2018). Evolution of the freshwater coastal
742 current at the Southern Tip of Greenland. *Journal of Physical Oceanography*, *48*(9).
743 https://doi.org/10.1175/JPO-D-18-0035.1

744 Luckman, A., Benn, D. I., Cottier, F., Bevan, S., Nilsen, F., & Inall, M. (2015). Calving rates at
745 tidewater glaciers vary strongly with ocean temperature. *Nature Communications*, *6*.
746 https://doi.org/10.1038/ncomms9566

747 Meredith, M. P., Brandon, M. A., Murphy, E. J., Trathan, P. N., Thorpe, S. E., Bone, D. G.,
748 Chernyshkov, P. P., & Sushin, V. A. (2005). Variability in hydrographic conditions to the
749 east and northwest of South Georgia, 1996-2001. *Journal of Marine Systems*.
750 https://doi.org/10.1016/j.jmarsys.2004.05.005

751 Millan, R., Rignot, E., Mouginot, J., Wood, M., Bjørk, A. A., & Morlighem, M. (2018).
752 Vulnerability of Southeast Greenland Glaciers to Warm Atlantic Water From Operation
753 IceBridge and Ocean Melting Greenland Data. *Geophysical Research Letters*, *45*(6).
754 https://doi.org/10.1002/2017GL076561

755 Millgate, T., Holland, P. R., Jenkins, A., & Johnson, H. L. (2013). The effect of basal channels
756 on oceanic ice-shelf melting. *Journal of Geophysical Research: Oceans*, *118*(12).
757 https://doi.org/10.1002/2013JC009402

758 Mortensen, J., Bendtsen, J., Motyka, R. J., Lennert, K., Truffer, M., Fahnestock, M., &
759 Rysgaard, S. (2013). On the seasonal freshwater stratification in the proximity of fast-
760 flowing tidewater outlet glaciers in a sub-Arctic sill fjord. *Journal of Geophysical*
761 *Research: Oceans*, *118*(3). https://doi.org/10.1002/jgrc.20134

762 Mortensen, J., Lennert, K., Bendtsen, J., & Rysgaard, S. (2011). Heat sources for glacial melt in
763 a sub-Arctic fjord (Godthåbsfjord) in contact with the Greenland Ice Sheet. *Journal of*
764 *Geophysical Research: Oceans*, *116*(1), 1–13. https://doi.org/10.1029/2010JC006528

765 Motyka, R. J., Cassotto, R., Truffer, M., Kjeldsen, K. K., van As, D., Korsgaard, N. J.,
766 Fahnestock, M., Howat, I., Langen, P. L., Mortensen, J., Lennert, K., & Rysgaard, S. (2017).
767 Asynchronous behavior of outlet glaciers feeding Godthåbsfjord (Nuup Kangerlua) and the
768 triggering of Narsap Sermia's retreat in SW Greenland. *Journal of Glaciology*, *63*(238).
769 https://doi.org/10.1017/jog.2016.138

Okubo, A. (1971). Oceanic diffusion diagrams. *Deep Sea Research and Oceanographic Abstracts*, *18*(8), 789–802. https://doi.org/10.1016/0011-7471(71)90046-5

O'Leary, M., & Christoffersen, P. (2013). Calving on tidewater glaciers amplified by submarine frontal melting. *Cryosphere*. https://doi.org/10.5194/tc-7-119-2013

Orsi, A. H., Whitworth, T., & Nowlin, W. D. (1995). On the meridional extent and fronts of the Antarctic Circumpolar Current. *Deep-Sea Research Part I*, *42*(5). https://doi.org/10.1016/0967-0637(95)00021-W

Penduff, T., le Sommer, J., Barnier, B., Treguier, A. M., Molines, J. M., & Madec, G. (2007). Influence of numerical schemes on current-topography interactions in 1/4° global ocean simulations. *Ocean Science*, *3*(4). https://doi.org/10.5194/os-3-509-2007

Schaffer, J., Kanzow, T., von Appen, W. J., von Albedyll, L., Arndt, J. E., & Roberts, D. H. (2020). Bathymetry constrains ocean heat supply to Greenland's largest glacier tongue. *Nature Geoscience*, *13*(3). https://doi.org/10.1038/s41561-019-0529-x

Sciascia, R., Straneo, F., Cenedese, C., & Heimbach, P. (2013). *Seasonal variability of submarine melt rate and circulation in an East Greenland fjord*. *118*(May), 2492–2506. https://doi.org/10.1002/jgrc.20142

Silvano, A., Rintoul, S. R., Peña-Molino, B., & Williams, G. D. (2017). Distribution of water masses and meltwater on the continental shelf near the Totten and Moscow University ice shelves. *Journal of Geophysical Research: Oceans*, *122*(3). https://doi.org/10.1002/2016JC012115

Slater, D. A., Nienow, P. W., Cowton, T. R., Goldberg, D. N., & Sole, A. J. (2015). Effect of near-terminus subglacial hydrology on tidewater glacier submarine melt rates. *Geophysical Research Letters*, *42*(8). https://doi.org/10.1002/2014GL062494

Slater, D. A., Nienow, P. W., Goldberg, D. N., Cowton, T. R., & Sole, A. J. (2017). A model for tidewater glacier undercutting by submarine melting. *Geophysical Research Letters*. https://doi.org/10.1002/2016GL072374

Sommer, U., & Lengfellner, K. (2008). Climate change and the timing, magnitude, and composition of the phytoplankton spring bloom. *Global Change Biology*. https://doi.org/10.1111/j.1365-2486.2008.01571.x

799 Soontiens, N., & Allen, S. E. (2017). Modelling sensitivities to mixing and advection in a sill-
800 basin estuarine system. *Ocean Modelling*, *112*, 17–32.
801 https://doi.org/10.1016/j.ocemod.2017.02.008

802 Soontiens, N., Allen, S. E., Latornell, D., le Souëf, K., MacHuca, I., Paquin, J. P., Lu, Y.,
803 Thompson, K., & Korabel, V. (2016). Storm Surges in the Strait of Georgia Simulated with
804 a Regional Model. *Atmosphere - Ocean*, *54*(1), 1–21.
805 https://doi.org/10.1080/07055900.2015.1108899

806 Staalstrøm, A., & Petter, L. (2016). Vertical mixing and internal wave energy fluxes in a sill
807 fjord. *Journal of Marine Systems*, *159*, 15–32.
808 https://doi.org/10.1016/j.jmarsys.2016.02.005

809 Straneo, F., & Cenedese, C. (2015). The dynamics of greenland's glacial fjords and their role in
810 climate. *Annual Review of Marine Science*, *7*. https://doi.org/10.1146/annurev-marine-
811 010213-135133

812 Straneo, F., Hamilton, G. S., Sutherland, D. A., Stearns, L. A., Davidson, F., Hammill, M. O.,
813 Stenson, G. B., & Rosing-asvid, A. (2010). Rapid circulation of warm subtropical waters in
814 a major glacial fjord in East Greenland. *Nature Geoscience*, *3*(February).
815 https://doi.org/10.1038/ngeo764

816 Umlauf, L., & Burchard, H. (2003). A generic length-scale equation for geophysical turbulence
817 models. *Journal of Marine Research*, *61*(2). https://doi.org/10.1357/002224003322005087

818 Venables, H. J., Meredith, M. P., & Brearley, J. A. (2017). Modification of deep waters in
819 Marguerite Bay, western Antarctic Peninsula, caused by topographic overflows. *Deep-Sea*
820 *Research Part II: Topical Studies in Oceanography*, *139*.
821 https://doi.org/10.1016/j.dsr2.2016.09.005

822 Ward, P. (1989). The distribution of zooplankton in an Antarctic fjord at South Georgia during
823 summer and winter. *Antarctic Science*, *1*(2). https://doi.org/10.1017/S0954102089000210

824 Wesławski, J. M., Kendall, M. A., Włodarska-Kowalczuk, M., Iken, K., Kedra, M., Legezynska,
825 J., & Sejr, M. K. (2011). Climate change effects on Arctic fjord and coastal macrobenthic
826 diversity-observations and predictions. In *Marine Biodiversity* (Vol. 41, Issue 1).
827 https://doi.org/10.1007/s12526-010-0073-9

Węsławski, J. M., Pedersen, G., Petersen, S. F., & Poraziński, K. (2000). Entrapment of macroplankton in an Arctic fjord basin, Kongsfjorden, Svalbard. *Oceanologia*, *42*(1), 57–69.

Winder, M., & Sommer, U. (2012). Phytoplankton response to a changing climate. In *Hydrobiologia*. https://doi.org/10.1007/s10750-012-1149-2

Young, E. F., Meredith, M. P., Murphy, E. J., & Carvalho, G. R. (2011). High-resolution modelling of the shelf and open ocean adjacent to South Georgia, Southern Ocean. *Deep-Sea Research Part II: Topical Studies in Oceanography*, *58*(13–16). https://doi.org/10.1016/j.dsr2.2009.11.003

Young, E. F., Thorpe, S. E., Banglawala, N., & Murphy, E. J. (2014). Variability in transport pathways on and around the South Georgia shelf, Southern Ocean: Implications for recruitment and retention. *Journal of Geophysical Research: Oceans*, *119*(1), 241–252. https://doi.org/10.1002/2013JC009348

Young, E., Murphy, E., & Trathan, P. (2016). High-resolution ocean modelling of the South Georgia and South Orkney Islands regions. *WG-EMM-16/15. CCAMLR Working Group on Ecosystem Monitoring and Management. Report of the XXXV Scientific Committee, Bologna, Italy.*